nature structural & molecular biology

Article

https://doi.org/10.1038/s41594-023-00959-z

Distinct structure and gating mechanism in diverse NMDA receptors with GluN2C and GluN2D subunits

Received: 16 November 2022

Accepted: 1 March 2023

Published online: 23 March 2023

Check for updates

Jilin Zhang[1,2,6], Ming Zhang[2,3,6], Qinrui Wang[4,6], Han Wen[4,6], Zheyi Liu[5], Fangjun Wang[5], Yuhang Wang[4], Fenyong Yao[1], Nan Song[1], Zengwei Kou[1], Yang Li[2,3], Fei Guo[2,3] & Shujia Zhu[1,2]

N-methyl-D-aspartate (NMDA) receptors are heterotetramers comprising two GluN1 and two alternate GluN2 (N2A-N2D) subunits. Here we report full-length cryo-EM structures of the human N1-N2D di-heterotetramer (di-receptor), rat N1-N2C di-receptor and N1-N2A-N2C tri-heterotetramer (tri-receptor) at a best resolution of 3.0 Å. The bilobate N-terminal domain (NTD) in N2D intrinsically adopts a closed conformation, leading to a compact NTD tetramer in the N1-N2D receptor. Additionally, crosslinking the ligand-binding domain (LBD) of two N1 protomers significantly elevated the channel open probability (Po) in N1-N2D di-receptors. Surprisingly, the N1-N2C di-receptor adopted both symmetric (minor) and asymmetric (major) conformations, the latter further locked by an allosteric potentiator, PYD-106, binding to a pocket between the NTD and LBD in only one N2C protomer. Finally, the N2A and N2C subunits in the N1-N2A-N2C tri-receptor display a conformation close to one protomer in the N1-N2A and N1-N2C di-receptors, respectively. These findings provide a comprehensive structural understanding of diverse function in major NMDA receptor subtypes.

N-methyl-D-aspartate (NMDA) receptors display functional heterogeneity, with N2C and N2D subtypes that are distinct from the N2A and N2B subtypes with respect to their gating activity and biophysical and pharmacological properties[1–3]. The N2C and N2D subunits show close evolutionary conservation[4], with N2C- and N2D-containing receptors exhibiting low channel activity, high agonist potency, less magnesium block and reduced calcium permeability as compared to the N2A- and N2B-containing receptors[2]. N2A and N2B are dominantly expressed in the cerebral cortex and hippocampus, whereas N2D is more restricted to the thalamus and hypothalamus, and N2C mainly exists in the cerebellum and olfactory bulb[5]. At the cellular level, N2C is predominately expressed in cerebellar granule cells[5,6], and both N2C and N2D are enriched in the GABAergic interneurons[7,8]. Under physiological conditions, both N2C- and N2D-containing NMDA receptors are crucial for the excitation–inhibition balance of neuronal activity[9]. Dysfunctions of these receptors are involved in neurological and psychiatric diseases[10–15]. For example, astrocytic N2C-containing NMDA receptors in the nucleus accumbens mediate cocaine preference and neuroadaptations[16], and N2D-containing receptors influence emotional behavior through the regulation of cell-specific synaptic transmission[17]. Accordingly, molecules that selectively target N2C- and N2D-containing NMDA receptors could be powerful tools for probing brain functions that involve these receptor subtypes, with regional

[1]Institute of Neuroscience, State Key Laboratory of Neuroscience, CAS Center for Excellence in Brain Science and Intelligence Technology, Chinese Academy of Sciences, Shanghai, China. [2]University of Chinese Academy of Sciences, Beijing, China. [3]Center for Neurological and Psychiatric Research and Drug Discovery, State Key Laboratory of Drug Research, Shanghai Institute of Materia Medica, Chinese Academy of Sciences, Shanghai, China. [4]DP Technology, Beijing, China. [5]CAS Key Laboratory of Separation Sciences for Analytical Chemistry, Dalian Institute of Chemical Physics, Chinese Academy of Sciences, Dalian, China. [6]These authors contributed equally: Jilin Zhang, Ming Zhang, Qinrui Wang, Han Wen. e-mail: shujiazhu@ion.ac.cn

https://doi.org/10.1038/s41594-023-00959-z

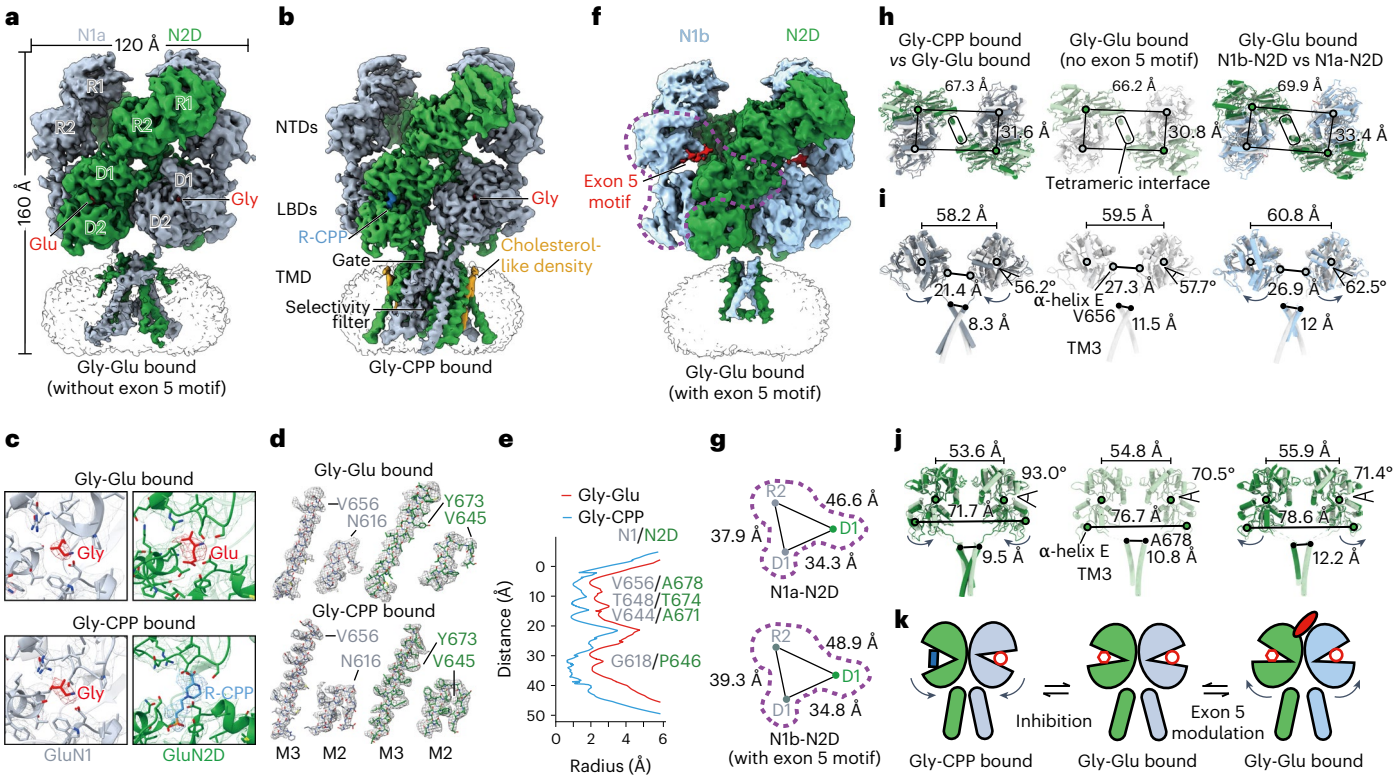

Fig. 1 | Molecular architecture and functional transition of the N1-N2D receptor. a,**b**, Cryo-EM structures of the N1-N2D receptor in Gly-Glu-bound (**a**) and Gly-CPP-bound (**b**) states. The electron density of agonists glycine and glutamate (Gly and Glu, red) and antagonist R-CPP (blue) are highlighted. **c**, Zoom-in views of the N1a- (gray) and N2D-LBD (green) clefts, with the EM density and structural coordinate for Gly (red), Glu (red) and R-CPP (cyan). **d**, Electron densities of the M2 and M3 helices for N1a and N2D of N1a-N2D receptors in the Gly-Glu and Gly-CPP states. **e**, HOLE analysis of the N1a-N2D receptor in the Gly-Glu and Gly-CPP states. Pore residuals of N1a and N2D are represented next to the corresponding location. **f**, Cryo-EM structure of the N1b-N2D receptor in the Gly-Glu bound state, with the presence of the exon-5 motif (with polypeptide D205-P210 visible) colored in red. The exon-5 motif-binding interface formed by N1-R2, N1-D1 and N2D-D1 lobes are outlined in violet. **g**, Diagram illustrating the center-of-mass (COM) distance with a triangle geometry connecting the N1-R2, N1-D1 and N2D-D1 lobes, with (lower panel) or without (upper panel) the exon-5 motif. **h**–**j**, Structural analysis of the top–down view of the tetrameric NTD (**h**) and side view of the two N1 (**i**) and N2D (**j**) protomers. The COM of each lobe, domain and α-helix E (P670-R673 for N1 and R696-Q699 for N2D) is shown as an open circle. Cα atoms of $N1^{A652}$ and $N2^{A678}$ in the gate are indicated by filled circles. Rounded rectangles in **h** indicate the NTD tetrameric interface. The dihedral angles indicating the opening–closure degree of the LBD are assessed by connecting the Cα of I403, S688, V735 and A715 in N1 and of P124, E525, S309 and E169 in N2D, respectively. Arrows indicate the conformational changes of Gly-CPP or the exon-5 motif modulated state receptors compared to the Gly-Glu state. **k**, Cartoon illustration of the conformational transition of the N1-N2D receptor among Gly-Glu, Gly-CPP and the exon-5 motif modulated states.

and cell-type specificity. In the past decade, the structures of N2A- and N2B-containing receptors have been extensively characterized, providing a molecular basis for understanding NMDA-receptor function[18–26]. However, the full-length structures and gating mechanisms of N2C- and N2D-containing NMDA receptors remain elusive. By combining cryo-EM, in silico calculations, mass spectrometry, biochemistry and single-channel recording, we here explored the structural architecture, gating transition and subtype-specific pharmacology in N1-N2D and N1-N2C di-receptors and the N1-N2A-N2C tri-receptor.

Intact N1-N2D receptor structures and functional transition

We first co-expressed constructs encoding the C-terminal-domain (CTD) truncated human N2D and N1a (without RNA-splicing exon 5) in HEK293S cells, then purified the tetrameric N1a-N2D di-receptors (Extended Data Fig. 1a–d). We solved the cryo-EM structures of the N1a-N2D receptor in complex with co-agonists glycine and glutamate (Gly-Glu), or with glycine and competitive antagonist R-CPP (Gly-CPP) (Fig. 1a,b and Table 1). During data-processing, application of *C*1 or *C*2 symmetry for three-dimensional (3D) refinement yielded two maps with a similar conformation (Extended Data Fig. 1e,f). We thus speculated that the N1-N2D di-receptor is likely to adopt an overall two-fold symmetry, perpendicular to the plane of the plasma membrane. Our final cryo-EM maps with *C*2 symmetry yielded resolutions of 4.0 Å and 3.7 Å for the Gly-Glu and Gly-CPP states, respectively (Extended Data Fig. 1g–j).

Globally similar to the bouquet-shaped N1-N2A and N1-N2B di-receptors[18–23], the N1-N2D receptor is assembled as a heterotetramer with two N1 peripheral and two N2D proximal to the central axis, top–down-viewed from the NTD layer (Fig. 1a,b). Topologically, the clamshell-like NTD (R1 plus R2 lobes) is distal to the membrane on the top, with the transmembrane domain (TMD) embedded in the lipid bilayer, and sandwiched between the bi-lobe ligand-binding domain (LBD; D1 plus D2) harboring the agonist binding pocket. The swapping feature of dimer association between NTDs and LBDs[18,19] was also present in the N1-N2D receptors. In both maps, we could visualize the electron densities at the cleft of N1-LBD for Gly, and of N2D-LBD for Glu and R-CPP (Fig. 1c). Both maps enabled us to build most of the secondary structures, including the M3 and M2 helices that formed the ion channel gate and selectivity filter (Fig. 1d). HOLE analysis revealed an ion channel gate in the Gly-Glu and Gly-CPP states with a smallest radius of ~2 Å and <1 Å (Fig. 1e), respectively, indicating that the Gly-Glu and Gly-CPP bound receptors are likely to be trapped in the inactive and inhibited states, respectively. We also determined the structure

https://doi.org/10.1038/s41594-023-00959-z

Table. 1 | Cryo-EM data collection, refinement and validation statistics for N1-N2D receptors

	N1a-N2D (Gly-Glu) (EMDB-33792; PDB 7YFL)	N1a-N2D (Gly-CPP) (EMDB-33788; PDB 7YFF)	$N1a^{E698C}$-N2D (C-C) (EMDB-33795; PDB 7YFO)	$N1a^{E698C}$-N2D (Non C-C) (EMDB-33798; PDB 7YFR)	N1b-N2D (Gly-Glu) (EMDB-33793; PDB 7YFM)
Data collection and processing					
Magnification	22,500	81,000	81,000	81,000	105,000
Voltage (kV)	300	300	300	300	300
Electron exposure (e^{-}/Å^2)	60	60	60	60	60
Defocus range (μm)	−1.5 ~ −2.5	−1.5 ~ −2.5	−1.5 ~ −2.5	−1.5 ~ −2.5	−2.0 ~ −2.5
Pixel size (Å)	1.067	1.071	1.071	1.071	0.803
Symmetry imposed	*C2*	*C2*	*C2*	*C2*	*C2*
Initial particle images (no.)	505,204	535,387	470,935	470,935	678,197
Final particle images (no.)	232,194	142,841	91,328	143,824	98,449
Map resolution (Å)	4.0	3.7	6.4	4.3	5.1
FSC threshold	0.143	0.143	0.143	0.143	0.143
Map resolution range (Å)	3.88–10.78	3.18–8.70	4.85–12.34	3.45–11.37	3.85–10.24
Refinement					
Initial model used (PDB code)	6WI1	6WI1	6WI1	6WI1	6WI1
Model resolution (Å)	4.18	3.74	7.28	4.29	6.76
FSC threshold	0.5	0.5	0.5	0.5	0.5
Map sharpening *B* factor (Å^2)	−220	−150	−220	−250	−230
Model composition					
Nonhydrogen atoms	19,908	21,790	18,288	19,084	18,836
Protein residues	2,770	3,018	2,542	2,670	2,518
Ligands	20	12	0	16	0
B factors (Å^2)					
Protein	35.37	68.39	416.37	109.51	234.37
Ligand	20	81.13	0	20	0
R.m.s. deviations					
Bond lengths (Å)	0.004	0.004	0.002	0.007	0.003
Bond angles (°)	0.587	0.611	0.533	0.632	0.641
Validation					
MolProbity score	1.80	1.99	2.02	1.85	2.01
Clashscore	6.47	8.68	12.28	8.69	10.16
Poor rotamers (%)	0.34	0	0.06	0.12	0
Ramachandran plot					
Favored (%)	93.02	93.02	93.73	93.96	92.23
Allowed (%)	6.84	6.78	6.10	5.81	7.69
Disallowed (%)	0.14	0.2	0.16	0.23	0.08

of the N1b-N2D receptor in the Gly-Glu bound state in the presence of N1-splicing cassette exon 5 at 5.1 Å resolution (Fig. 1f, Extended Data Fig. 2 and Table 1). Electron density of the exon-5 cassettes was visible between α-helix 6 and β-sheet 7 on N1-NTD, similar to that found in the N1b-N2B receptor structure[27]. Compared with the N1a-N2D receptor, the exon-5 polypeptide enlarged the edge distances of the triangle formed by N1-R2, N1-D1 and N2D-D1 lobes (Fig. 1g).

By comparing these biologically relevant structures, we noticed that the NTDs displayed similar configurations, especially with their tetrameric interfaces uniformly formed by the α5-helices of N2D-NTDs (Fig. 1h). By comparing Gly-Glu and Gly-CPP bound states, antagonist R-CPP binding to the N2D-LBD cleft opened the clamshell by 23.5° and subsequently pulled together the D2-D2 lobes, leading to a shortened distance between the two gate-linked α-helices E in the LBD by 5.9 Å in N1 and 5 Å in the N2D subunits and between the two Cα of the gate residues by 3.2 Å in N1 and 1.3 Å in the N2D subunits, respectively (Fig. 1i,j). Moreover, in the presence of exon 5, all four chains moved away from the central axis, as indicated by the expanded center-of-mass (COM) distances of two N1b- and two N2D-LBDs by 1.3 Å and 1.1 Å, respectively, as well as two α-helices E in N2D-LBDs that were pushed away by 1.9 Å in the N1b-N2D receptor (Fig. 1i,j). We suggest that this conformational movement triggered by exon 5 could account for more active gating properties in N1b-N2D receptors[27,28]. These data imply that the molecular mechanisms of antagonist inhibition and splicing exon-5 modulation are conserved among the N1-N2D, N1-N2A[25] and N1-N2B[24,27] di-receptors (Fig. 1k).

https://doi.org/10.1038/s41594-023-00959-z

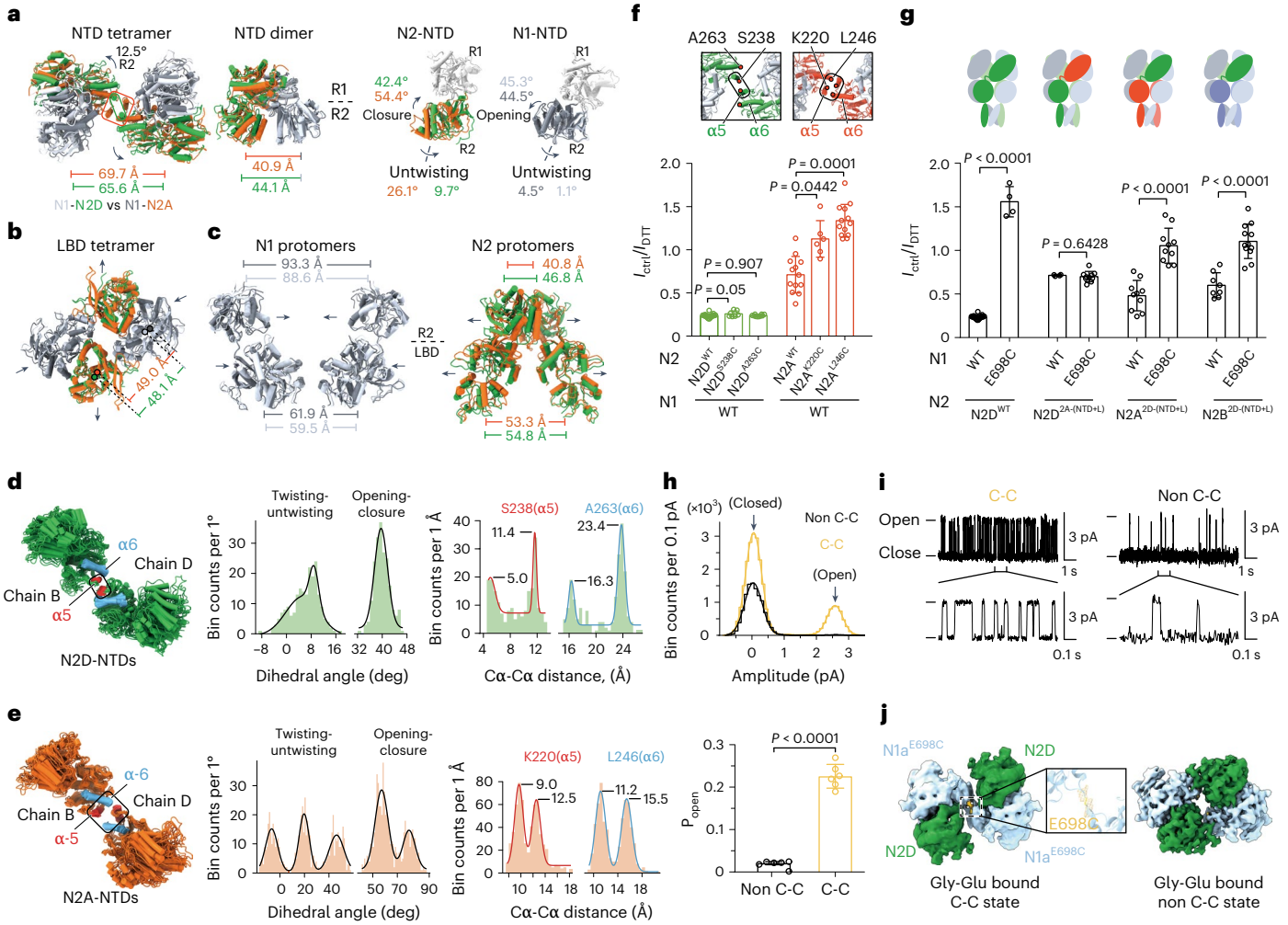

Fig. 2 | NTD and LBD function in the N1-N2D receptor. a–**c**, Structural comparison of Gly-Glu bound N1-N2D and N1-N2A (PDB 6MMP; ref. [22]) di-receptors, as indicated. Lines indicate COM distances between domains or lobes, angles indicate dihedral closed–open or twisted–untwisted conformations of the NTDs, with colors correlated to the corresponding subunits. Arrows indicate the conformational change from N1-N2A to N1-N2D di-receptors. **d**,**e**, MD simulations of N1-N2D (**d**) and N1-N2A (**e**) receptors, with the trajectory of the N2D-NTDs (upper panels) and N2A-NTDs (lower panels) shown on the left. The middle and right panels show histogram distributions of the open–closed and twisted–untwisted dihedral angles of GluN2-NTD, and the Cα-Cα distance for the marked residues from the α5 and α6 helices. **f**,**g**, DTT-induced current amplitude changes on WT and mutant receptors. The top panels show the NTD tetrameric interfaces of N2A and N2D (**f**) and a cartoon illustration of WT and chimeric receptors (**g**), with N2D, N2A and N2B subunits colored in green, orange and violet, respectively. The shown relative current values (before and after DTT treatment), from left to right, are 0.24 ± 0.02 (n = 19), 0.26 ± 0.03 (n = 7), 0.24 ± 0.01 (n = 10), 0.72 ± 0.21 (n = 13), 1.13 ± 0.15 (n = 6) and 1.34 ± 0.19 (n = 13) in **f**, and 0.24 ± 0.02 (n = 19), 1.56 ± 0.17 (n = 4), 0.71 ± 0.01 (n = 4), 0.70 ± 0.06 (n = 10), 0.48 ± 0.17 (n = 10), 1.05 ± 0.20 (n = 10), 0.60 ± 0.14 (n = 8) and 1.10 ± 0.20 (n = 12) in **g**. **h**, Amplitude histograms fitted by two Gaussian distributions and the statistics of Po, for crosslinked (marked as C-C, 0.226 ± 0.028, n = 6) and non-crosslinked (marked as non C-C, 0.021 ± 0.002, n = 6) N1^{E698C}-N2D receptors. **i**, Representative single-channel recording traces of C-C and non C-C receptors. **j**, Top–down view of the electron density of LBDs in the N1^{E698C}-N2D receptor in crosslinked and non-crosslinked states. Yellow mesh highlights the density of crosslinked E698C residues from two N1 protomers. All data are presented as mean ± s.d.; n numbers imply independent oocytes or proteoliposomes. P values are determined by one-way analysis of variance (ANOVA) with Tukey's multiple comparison test in **f** and by two-tailed unpaired Student's t-test in **g** and **h**.

Dominant negative role of N2D-NTD

As the N1-N2A and N1-N2D di-receptors represent two extremes of biophysical property in NMDA receptors[2], we compared their structures under the same condition of a Gly-Glu bound state. Overall, the tetrameric NTD in the N2D receptors underwent a counterclockwise rotation and adopted a more compact configuration as compared to that in N2A receptors (Fig. 2a). Specifically, the N2D-NTD intrinsically adopts a closer (by 12°) and more untwisted (by 16.4°) clamshell than N2A-NTD (Fig. 2a). Molecular dynamics (MD) simulations further indicated that the N2D-NTD is less mobile than the N2A-NTD, as assessed by angle measurements of the twisting–untwisting and opening–closure (Fig. 2d,e). This rigid conformation of N2D-NTD is in line with the proposals of previous functional studies[29,30]. The configuration of N2D-NTD leads to separation of the R2-R2 lobes within the NTD heterodimer (Fig. 2a) and a '1-Knuckle' (solely formed by α5-α5 helices) conformation at the tetrameric interface in the N1-N2D receptor (Fig. 2d), in contrast to the '2-Knuckle' (composed of α5 and α6 helices) conformation in the N1-N2A receptor[22] (Fig. 2e). Notably, our structure for the N1-N2D receptor displays a similar NTD conformation as the zinc-inhibited N1-N2A receptor trapped in the '1-Knuckle' state[22] (Extended Data Fig. 3a,b), explaining the reason why N2D-NTD has a low affinity for zinc[31].

Next, MD simulations further illustrated that the tetrameric interface is constantly formed by two α5 helices in the N2D-NTDs (Fig. 2d). In two independent trajectories, the two α5 helices displayed closer contact, indicated by the Cα-Cα distance of two

S238 residues, whereas the two α6 helices showed a consistent separation, shown by the long Cα-Cα distance of two A263 residues (Fig. 2d). To validate these structural observations we introduced a cysteine substitution on N2D^{S238} in the α5 helix (Fig. 2f) and found a spontaneously formed band corresponding to the N2D-N2D homodimer in N1-N2D^{S238C} receptors (Extended Data Fig. 3c,g). Two-electrode voltage-clamp (TEVC) recordings on *Xenopus* oocytes showed that the N1-N2D^{S238C} receptors exhibit a relative Po (measured by the kinetics of MK-801-induced current inhibition[32,33]; Extended Data Fig. 3i) and dithiothreitol (DTT)-induced current amplitude reduction (Fig. 2f), similar to that in N1-N2D wild-type (WT) receptors. As a control, it was found that N1-N2D^{A263C} receptors could not form disulfide crosslinking (Extended Data Fig. 3g) and exhibited no impact on channel activity (Fig. 2f). In contrast, cysteine replacement on homologous sites of the α5 and α6 helices on the N2A subunit significantly boosted the channel activity after DTT reducing treatment, as compared to N1-N2A WT receptors (Fig. 2f and Extended Data Fig. 3e,f). Taken together with the results of previous studies[29,30], we suggest that N2D-NTD is consistently stabilized in the less-twisted and closed conformation, which has a dominant-negative impact on N1-N2D channel gating.

Functional NTD-LBD cooperativity

Based on the structural comparison, the NTD configuration was synchronously coupled to the downstream LBD layer (Fig. 2b,c), with more constrained N1-LBDs and more expanded N2D-LBDs (Fig. 2b,c) than in N1-N2A receptors. To check whether crosslinking the LBD interface would affect the channel gating of the N1-N2D receptors, we introduced an individual cysteine substitution at the sites of V697, E698 and L699 on the N1-LBD (Extended Data Fig. 3d). The N1$^{C744A\text{-}C798A}$-N2D receptors without endogenous redox sensor[34] exhibited no change in current amplitude, but the N1$^{C744A\text{-}C798A\text{-}E698C}$-N2D receptors showed a most marked inhibition by ~2.4-fold after DTT treatment (Extended Data Fig. 3k). Next, we found that the N1^{E698C}-N2D receptors displayed tenfold faster MK-801 inhibition kinetics (Extended Data Fig. 3j) than the N1-N2D WT receptors, as well as a significant current reduction after DTT treatment (Extended Data Fig. 3l). Biochemical analysis further demonstrated that the N1 subunits spontaneously form a homodimer in the N1^{E698C}-N2D receptors (Extended Data Fig. 3h). In addition, the Gly and Glu sensitivities of the N1^{E698C}-N2D receptors significantly declined by 170- and 4-fold, respectively (Extended Data Fig. 3m). Together, we have demonstrated that a single cysteine replacement at E698 of the N1 subunit dramatically switches the channel of the N1-N2D receptors from a low- to high-activity state.

To explore whether the NTD and LBD conformation is functionally coupled, we swapped the NTD plus the NTD-LBD linker between the N2D and N2A or N2B subunits. The N1^{E698C}-N2D receptors could be spontaneously locked in a super-active state (Fig. 2g and Extended Data Fig. 4j–l). Conversely, the N1^{E698C}-N2D$^{2A\text{-}(NTD+L)}$ receptors lost their current boosting effect in response to the DTT treatment and showed no significant difference as N1-N2D$^{2A\text{-}(NTD+L)}$ receptors (Fig. 2g). Previous studies have reported that the N1^{E698C}-N2A receptors decreased the channel activity by approximately twofold, but the N1^{E698C}-N2B receptors had no significant effect on the reducing reagent compared to the corresponding WT receptors[35,36]. Strikingly, both the N1^{E698C}-N2A$^{2D\text{-}(NTD+L)}$ and N1^{E698C}-N2B$^{2D\text{-}(NTD+L)}$ chimeric receptors showed significant current reinforcement in response to DTT reduction, in comparison with the corresponding chimeric receptors with no cysteine substitution on the N1^{E698} site (Fig. 2g). These data confirm that the conformation of N2D-NTD allosterically controls the functional crosslinking of tetrameric LBDs.

Functionally and structurally trapping N1^{E698C}-N2D receptors

We next purified the protein of CTD-deleted N1^{E698C}-N2D receptors and found a spontaneously crosslinked complex of ~250 kDa corresponding to N1 homo-dimers (Extended Data Fig. 4a,b). We reconstructed the purified N1^{E698C}-N2D protein into the proteoliposomes and performed single-channel recordings to evaluate the absolute Po. We found two independent channel activity profiles, with one population displaying a hyperactive (C-C state) Po of 0.226 ± 0.028 and the other (non C-C state) 0.021 ± 0.002 (Fig. 2h,i). The latter was close to the value previously found for WT N1-N2D receptors[28]. Based on these results, we concluded that the receptor in the C-C state was probably trapped in a hyperactive conformation.

We determined the structure of the N1^{E698C}-N2D receptors in complex with Gly-Glu and found two classes of EM map with different LBD conformations (Fig. 2j, Extended Data Fig. 4c–e and Table 1). One structure at 6.4-Å resolution displayed two tethered N1-LBD protomers that were crosslinked at the E698C residue (named the 'C-C state' in Fig. 2j). The other structure at 4.3-Å resolution with a non-crosslinked N1-LBD exhibited a similar conformation as the Gly-Glu bound WT receptors, with a root-mean-squared deviation (r.m.s.d.) of 1.3 Å ('non C-C state'; Fig. 2j). A structural comparison of the Gly-Glu and C-C states revealed that disulfide crosslinking through N1^{E698C}-N1^{E698C} glued together two N1-LBDs and expanded two N2D-LBD protomers, as indicated by the COM distances (59.5 Å for Gly-Glu versus 56.3 Å for C-C for N1; 55.5 Å for Gly-Glu versus 65.1 Å for C-C for N2D; Extended Data Fig. 4f). Strikingly, the two α-helices E in the N2D-LBDs (directly linked to M3) underwent a large outward movement, with their COM distance changed from 76.9 Å in the WT receptor to 89.7 Å in the C-C state receptor. So far, among all the resolved NMDA-receptor structures, our C-C state receptors exhibit the largest separation of the D2-D2 lobes of the two N2 subunits (Extended Data Fig. 4g). Taken together, these functional and structural results are in line with each other, proving that a single disulfide crosslinking by GluN1^{E698C} at the tetrameric interface of LBD could convert the low Po of the N1-N2D receptors to a high active state.

Asymmetric and symmetric structures of the N1-N2C di-receptor

The N1-N2C receptors display distinctive biophysical properties, including low channel open probability, modest desensitization and two main conductance levels[37]. As no structural information is currently available, we purified the protein of the CTD-truncated N1-N2C receptor (Extended Data Fig. 5a,b) and elucidated its cryo-EM structures in the presence of Gly-Glu (Fig. 3a–c, Extended Data Fig. 5c and Table 2). After multiple rounds of 3D classification, the entire dataset yielded three classes, with a major class (87% population) and an intermediate class (5.5% population) in the asymmetric conformation and a minor class (7.5% population) in the symmetric conformation. The asymmetric feature was mainly characterized by the geometry viewed from top–down NTDs (Extended Data Fig. 5c). We thus carried out 3D refinement for the major and minor classes with *C*1 and *C*2 symmetry, respectively, and obtained two density maps of the N1-N2C di-receptor at 3.6 Å and 4.3 Å resolutions, respectively (Fig. 3b,c and Extended Data Fig. 5c). Overall, the TMD signal in these structures is not well-resolved, which is presumably linked to the evidence from single-channel recordings that shows that the channel gate of the N1-N2C di-receptors transits among multiple inactive and open states in response to the binding of Gly-Glu[37]. Note that there is a subclass isolated from the major class that displays a certain signal of the M2 and M3 helices (Fig. 3a). To validate the subunit identity, we performed mass spectrometry with the purified protein and confirmed 11 and 5 glycans on the N1 and N2C subunits, respectively, in agreement with signals on the EM map for sugar moieties (Extended Data Fig. 6). Therefore, we have confirmed that the N1-N2C di-receptor is globally assembled in a N1-2C-N1-2C pattern, with a dimer-of-dimer structure exhibiting a domain swapping feature as in other N1-N2 subtypes[18–23] (Fig. 3a–c).

In the major class, the electron density of the extracellular domains (ECDs) was of decent quality, and Gly and Glu were clearly visible

https://doi.org/10.1038/s41594-023-00959-z

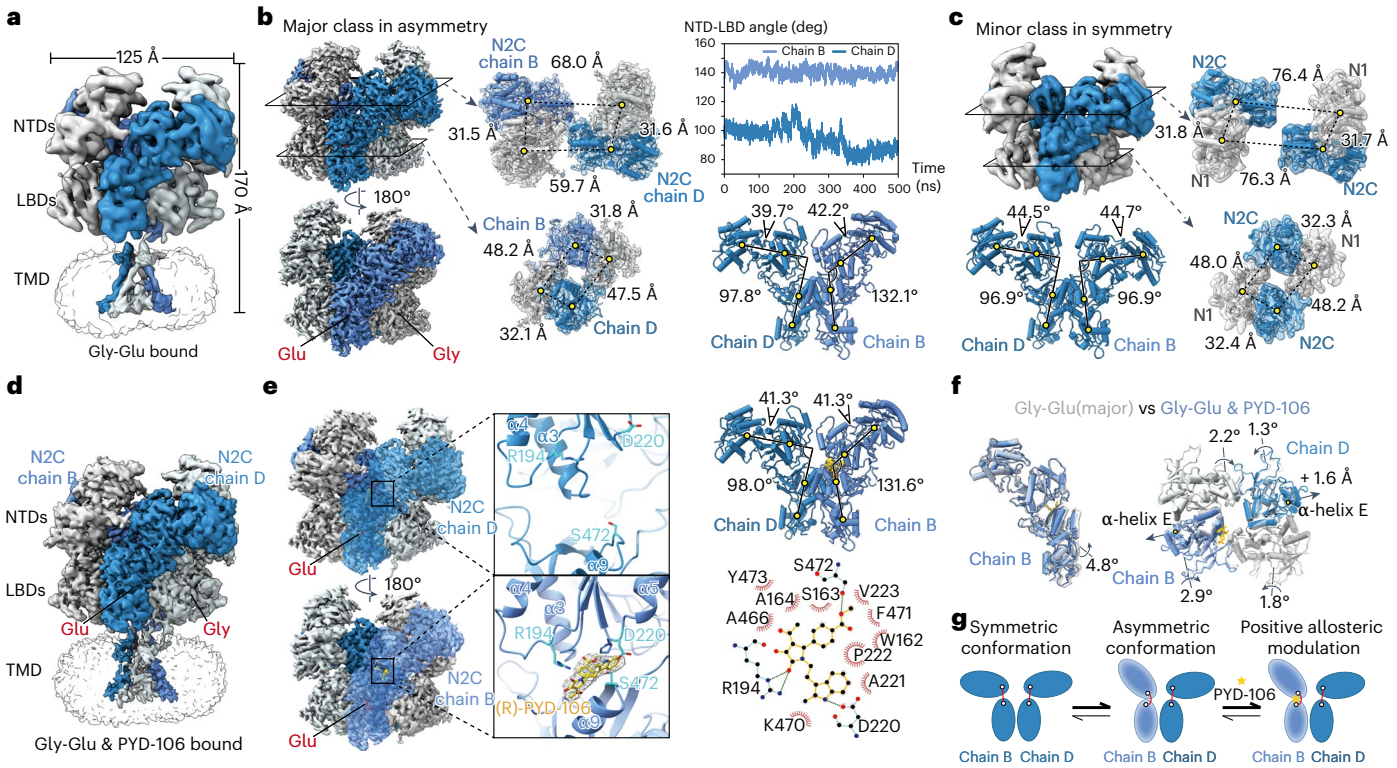

Fig. 3 | Cryo-EM structures and unique allosteric modulation of the N1-N2C di-receptor. a,**d**, Intact cryo-EM structures of the N1-N2C di-receptors in the Gly-Glu (**a**) and Gly-Glu and PYD-106 (**d**) bound states. Both maps are subclasses isolated from the respective major class (Extended Data Figs. 5 and 7). The N1 and N2 subunits are marked as chain A/C and chain B/D, respectively. The agonists glycine and glutamate are shown in red. **b**,**c**, Structural analysis of the N1-N2C di-receptors in the major asymmetric (**b**) and minor symmetric (**c**) conformations. Side views of the EM maps and top–down views of the NTD and LBD tetramers are illustrated. Conformation comparisons between the two N2C subunits are indicated by vector angles connecting the COMs of R2 and R1, and the D1 and D2 lobes of the N2C protomers. R.m.s.d trajectories for two N2C protomers (chains B and D) based on the asymmetric structure along the total simulation of 500 ns are shown in the middle panel. **e**, Left: structural analysis of the N1-N2C di-receptors in the Gly, Glu and PYD-106 bound states. The frontal N2C is transparent for clarity. Middle: magnified view of the NTD-LBD interface for the two N2C protomers. The EM density of (*R*)-PYD-106 is shown (in gold) at the NTD-LBD interface of chain B. Residues forming hydrogen-bond interactions with PYD-106 are shown as cyan sticks. Right: conformation analysis of two N2C subunits and detailed interactions between PYD-106 and N2C, as analyzed by LigPlot⁺. **f**, Conformational change induced by positive allosteric modulation of PYD-106. Left: NTD superimposed on the N2C subunits (chain B in the asymmetric class) of Gly-Glu (white) and PYD-106 (blue) bound structures, with the LBD rotation angle indicated. Right: superimposition of the LBD layers of the Gly-Glu (major class) and PYD-106 bound states, with the inward rolling degrees of the four LBDs and the distance changes between the two α-helices E of the N2C subunits, indicated upon PYD-106 binding. **g**, Cartoon illustration for the dynamic transition of the N1-N2C di-receptor among the symmetrical (minor), asymmetrical (major) and PYD-106 bound conformations.

within the LBD clamshells of N1 and N2C, respectively (Fig. 3b and Extended Data Fig. 7a,b). Notably, both heterodimer subunits exhibited a largely asymmetrical configuration. On the NTD layer, in particular, the inter-subunit COM distance between chains A and D (59.7 Å) was substantially smaller than that between chains B and C (68.0 Å; Fig. 3b). As controls, the two individual N1- or N2C-NTD protomers and the two heterodimers exhibited conformational similarity (Extended Data Fig. 7c). On the LBD layer, four LBDs exhibited a pseudo twofold symmetry (Fig. 3b and Extended Data Fig. 7d). We attributed this transition from asymmetric NTD and symmetric LBD to different conformations of the NTD-LBD linker in the two N2C subunits (Fig. 4d). In this major class, two N2C protomers of identical sequence exhibited distinct conformations, with an NTD-LBD angle of 132.1° in chain B and 97.8° in chain D. MD simulations of this asymmetric structure revealed that both N2C subunits exhibited a stable asymmetric conformation, as indicated by the minimum changes in NTD-LBD angles (Fig. 3b) and small fluctuation in r.m.s.d. values (Extended Data Fig. 5d).

In the minor class, we found that both N2C subunits adopt the conformation of chain D in the major class, characterized by an NTD-LBD angle of 96.9° (Fig. 3c). On the NTD layer, the two NTD heterodimers are largely splayed from each other with an inter-subunit COM distance of 76.4 Å (Fig. 3c). Moreover, the intermediate class exhibited a conformation situated between the major and minor classes. Aligning the maps among these three classes showed a rotation of one NTD heterodimer by 33.8° (Extended Data Fig. 5d). MD analysis showed that this symmetric conformation was highly mobile (with r.m.s.d. ranging from ~0.4 nm to more than 1.4 nm), with a tendency to shift its conformation to the asymmetric state (Extended Data Fig. 5d).

Notably, in the asymmetric structure, the NTD tetrameric interface formed by the two α-helices 5 from two N2C-NTDs was misaligned. Residue D220 at the bottom of α-helix 5 in chain D directly forms ionic bond interactions with R211 and R214 at the top of α-helix 5 in chain B (Extended Data Fig. 7e). The interface energy between the two N2C-NTDs is −9.075 REU (Rosetta energy units). By contrast, in the symmetric structure, the two N2C-NTDs are physically separated, with the electrostatic repulsion presumably caused by two R214 residues on chain B and chain D (Extended Data Fig. 7e). Rosetta interface energy analysis also showed zero interaction energy between these two N2C-NTDs. We thus propose that the N1-N2C di-receptor can spontaneously transition between the symmetric and asymmetric conformations, with the asymmetric conformation being more energetically favorable (Fig. 3g).

https://doi.org/10.1038/s41594-023-00959-z

Table. 2 | Cryo-EM data collection, refinement and validation statistics for N2C-containing receptors

	N1a-N2C (asymmetric) (EMDB-33789; PDB 7YFG)	N1a-N2C (symmetric) (EMDB-34674; PDB 8HDK)	N1a-N2C (PYD-106 bound) (EMDB-33790; PDB 7YFH)	N1a-N2A-N2C (EMDB-33791; PDB 7YFI)
Data collection and processing				
Magnification	81,000	81,000	81,000	81,000
Voltage (kV)	300	300	300	300
Electron exposure ($e^-/Å^2$)	60	60	60	60
Defocus range (μm)	−1.2~−2.0	−1.2~−2.0	−1.2~−2.0	−1.2~−2.0
Pixel size (Å)	1.071	1.071	1.071	1.071
Symmetry imposed	*C*1	*C*2	*C*1	*C*1
Initial particle images (no.)	1,188,229	1,188,229	2,094,482	891,914
Final particle images (no.)	245,730	15,479	601,826	278,030
Map resolution (Å)	3.61	4.31	3.03	3.53
FSC threshold	0.143	0.143	0.143	0.143
Map resolution range (Å)	3.41–6.21	4.21–9.17	2.89–4.71	3.08–7.20
Refinement				
Initial model used (PDB code)	6WI1	6WI1	6WI1	6MMT
Model resolution (Å)	3.65	4.87	3.10	3.70
FSC threshold	0.5	0.5	0.5	0.5
Map sharpening *B* factor ($Å^2$)	−125	−134	−50	−125
Model composition				
Nonhydrogen atoms	21,222	20,901	21,289	24,138
Protein residues	2,620	2,608	2,620	2,980
Ligands	48	32	53	45
B factors ($Å^2$)				
Protein	38.18	278.15	90.65	135.75
Ligand	81.14	333.80	140.15	102.90
R.m.s. deviations				
Bond lengths (Å)	0.011	0.003	0.007	0.003
Bond angles (°)	1.113	0.703	0.808	0.672
Validation				
MolProbity score	1.94	2.21	1.79	1.96
Clashscore	10.43	19.91	7.48	8.80
Poor rotamers (%)	0.18	0.00	0.13	1.20
Ramachandran plot				
Favored (%)	93.92	93.71	94.42	93.59
Allowed (%)	5.88	6.02	5.35	6.00
Disallowed (%)	0.19	0.27	0.23	0.41

N2C-specific positive allosteric modulation

A series of pyrrolidinones (PYDs) have been identified as positive allosteric modulators (PAMs) specifically for N1-N2C di-receptors, with potency in the micromolar range[38]. Functional studies have revealed that the potentiation effect of PYD-106 is induced by one enantiomer[38] and is completely lost in the N1-N2A-N2C tri-receptors[39–41]. So far, the accurate binding site and allosteric mechanism of PYD-106 remain unknown. We thus tried to resolve the cryo-EM structure of the N1-N2C receptor in the presence of Gly-Glu and PYD-106. Finally, a cryo-EM map at 3.0-Å resolution was obtained, with no symmetry applied (Fig. 3d, Extended Data Fig. 8 and Table 2). In the map, a clear electron density was only found at the compact NTD-LBD interface of the N2C subunit in chain B, but not in chain D (Fig. 3e), which was not predicted by previous functional and modeling data[39,41].

The enantiomer of (*R*)-PYD-106 could perfectly fit into the geometry of the electron density, but (*S*)-PYD-106 was stoichiometrically unfavorable (Extended Data Fig. 9a). LigPlot$^+$ analysis showed that three pairs of hydrogen-bond interaction, between R194 and the carbonyl on pyrrolidinone, D220 and the nitrogen of the indole ring, and S472 and the methyl ester. These interactions stabilized the three aromatic nuclei of PYD-106 (Fig. 3e), in line with electrophysiological findings that mutation at any of the abovementioned residues resulted in the complete loss of PYD-106 potentiation[39,41]. Moreover, residues at the bottom of the R2 lobe (especially P222) and the top of the D1 lobe (A466 to Y473) formed hydrophobic interactions with PYD-106 (Fig. 3e).

The binding of PYD-106 resulted in a 4.8° rotation of the LBD relative to the NTD in the N2C of chain B and generated asymmetrical inward rolling of all four LBD clamshells (Fig. 3f). Consequently,

https://doi.org/10.1038/s41594-023-00959-z

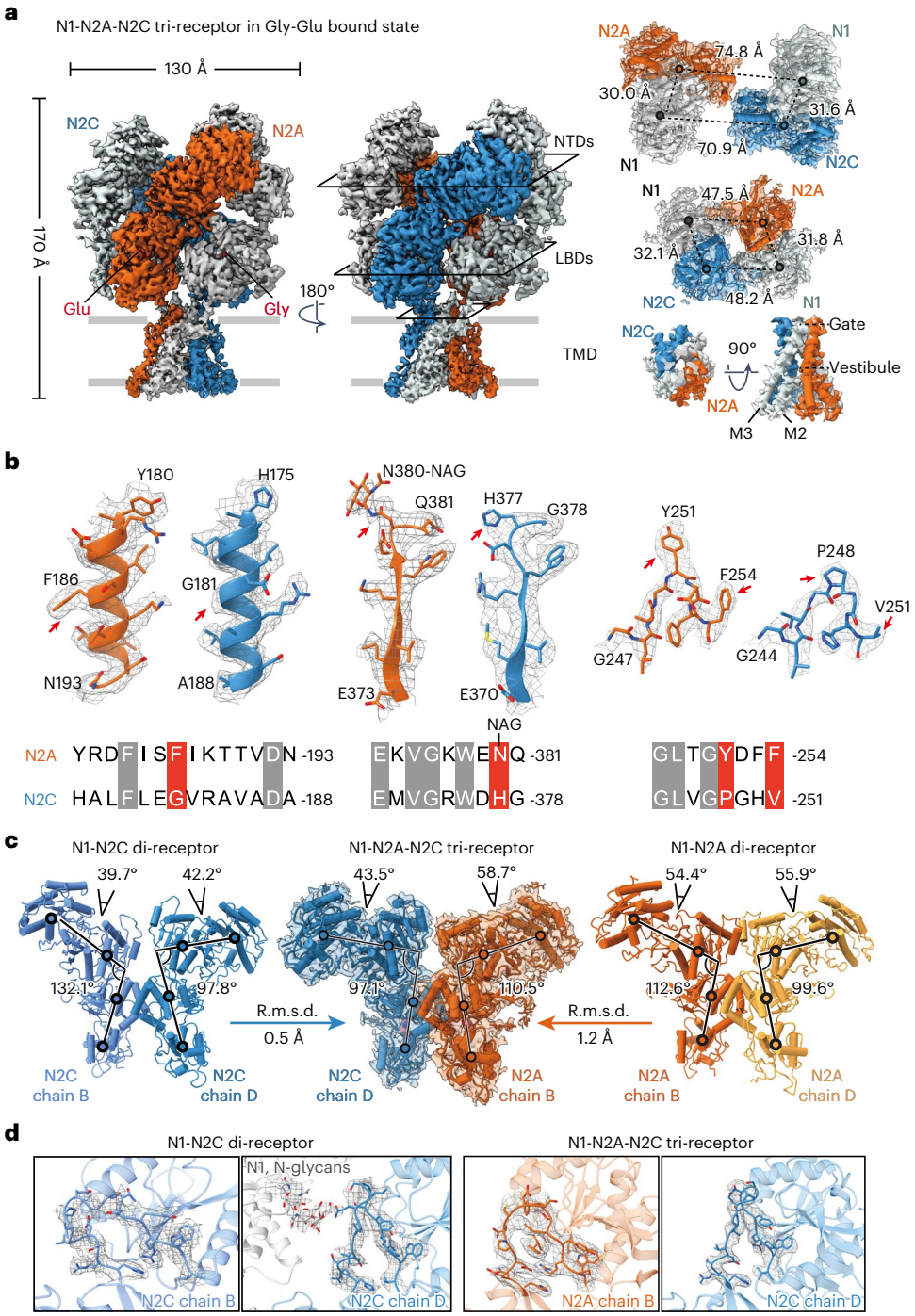

Fig. 4 | Structural analysis of the N1-N2A-N2C tri-receptor. a, Cryo-EM structures of the N1-N2A-N2C tri-receptor in the Gly-Glu bound state. Top–down views of the NTDs, LBDs and TMD are shown on the right. **b**, Local EM density illustration (top) and corresponding sequence alignment (bottom) of the N2A and N2C subunits in the tri-receptor. Homologous residues between the N2A and N2C subunits with different EM densities are indicated by red arrows. The glycosylation density is marked at the site of $N2A^{N380}$, in comparison to the non-glycosylated $N2C^{H377}$ site. **c**, Conformation comparison of N2A and N2C in the tri-receptor and respective di-receptors. The NTD-LBD angles and NTD clamshell opening angles are all indicated. The r.m.s.d. values for extracellular domain alignment for the N2A in the tri- and di-receptor (chain B versus chain D) are 1.2 versus 2.2 Å, and for the N2C in the tri- and di-receptor (chain B versus chain D) are 6.3 versus 0.5 Å, respectively. **d**, Zoomed views of the NTD-LBD linker density of the N2 subunits in the N1-N2C and N1-N2A-N2C receptors.

the allosteric binding of PYD-106 led to conformational changes in N2C-LBD, reflected by the 1.6-Å outward movement of α-helix E, which directly linked to the channel gate (Fig. 3f and Supplementary Video 1). To examine the basis of PYD-106 selectivity for the N1-N2C di-receptors, we performed sequence alignment and found that R194, D220 and S472 in N2C showed low conservation, with homologous residues in the N2A/2B/2D subunits (Extended Data Fig. 9b). Moreover, a structural comparison showed that only in chain B of the N1-N2C receptors does the NTD-LBD interface form an adequate R2-D1 contact area (indicated by the interface delta solvent accessible surface area (dSASA) of 908.4 $Å^2$), yielding the lowest interface binding energy (dG_separated of −7.7 REU) compared with those of the other N2

https://doi.org/10.1038/s41594-023-00959-z

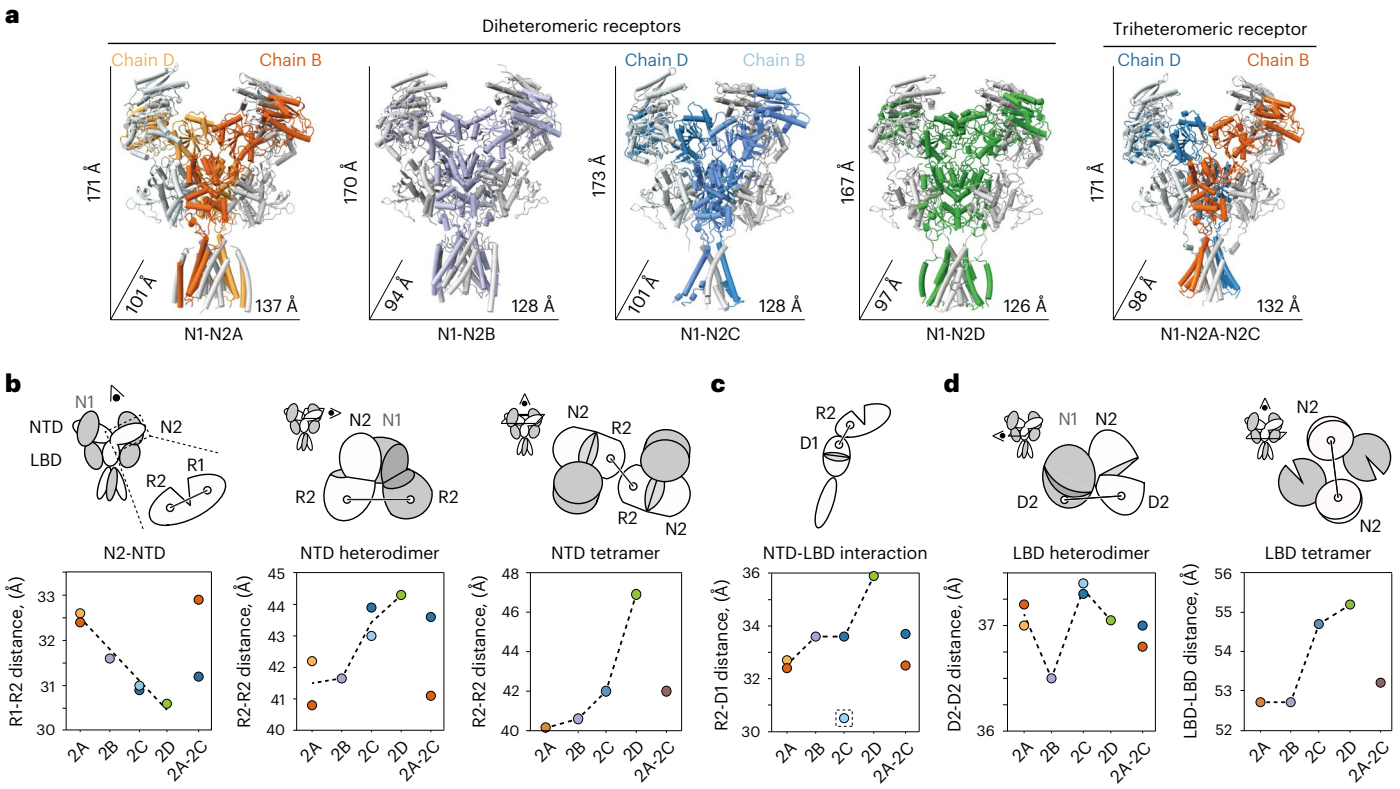

Fig. 5 | Comprehensive structural analysis of diverse NMDA receptors. a, A gallery of cryo-EM structures for N1-N2A (PDB 6MMP), N1-N2B (PDB 7EU8; ref. [26]), N1-N2C and N1-N2D di- and N1-N2A-N2C tri-receptors in the Gly-Glu bound state. **b**–**d**, Scatter diagrams of COM distance in various NMDA-receptor subtypes. In the schematic representation of the tetrameric NMDA receptor, N1 is colored in gray and N2 in white. Six parameters measuring the distance between the COMs of lobes and domains are indicated. For the asymmetric N1-N2A, N1-N2C di- and N1-N2A-N2C tri-receptors, two N2 subunits of chain B and chain D with different geometries were individually measured. For the symmetric N1-N2B and N1-N2D receptors, the mean values of parameters measured for chain B and chain D were used for plots. NTD conformations of the monomer, heterodimer and tetramer are indicated by COM distances of R1-R2 in N2, R2-R2 in the heterodimer and R2-R2 between the two N2-NTDs, respectively (**b**). The NTD-LBD conformation is characterized by the R2-D1 distance in the N2 subunit, with a dashed box indicating chain B of the N2C subunit in the N1-N2C di-receptors (**c**). LBD conformations of the dimer and tetramer are indicated by the COM distances of D2-D2 in the heterodimer and two N2-LBDs, respectively (**d**). Dashed lines connecting the parameters from N2A to N2D di-receptors show the tendency of conformational transition among these four major subtypes.

subunits (Extended Data Fig. 9c). Notably, the two N2C protomers also adopted an asymmetric conformation with NTD-LBD angles of 131.6° in chain B and 98.0° in chain D (Fig. 3e), consistent with the asymmetric conformation in the major class of Gly-Glu bound state (Fig. 3b). In summary, our data indicate that PYD-106 preferably locks the N1-2C di-receptor in the asymmetric conformation (Fig. 3g).

Architecture of tri-heteromeric N1-N2A-N2C receptor

Previous studies have proposed that N1-N2A-N2C tri-receptors are the dominant population in cerebellar granule cells, and these tri-receptors retain biophysical properties of both N1-N2A and N1-N2C di-receptors[6,40,42]. To explore its architecture, we fused His- and Strep-tags on N2A and N2C constructs, respectively, and isolated tri-receptors by two-step affinity chromatography. Western blotting analysis verified the presence of both N2A and N2C subunits in the purified tri-receptor proteins (Extended Data Fig. 10a,b). Eventually, we obtained a 3.5 Å resolution EM density map of the N1-N2A-N2C receptor in complex with Gly-Glu (Fig. 4a, Extended Data Figs. 7a and 10a,b and Table 2). Mass spectrometry revealed six and five glycans on the N2A and N2C subunits, respectively (Extended Data Fig. 6). The presence of glycans at the $N2A^{N380}$ position and absence at the homologous site of $N2C^{H377}$ clearly distinguish the N2A from the N2C subunits. Furthermore, our high-resolution map also provides clear signals of side chains to authenticate the N2A and N2C subunits, based on non-conserved NTD sequences (Fig. 4b). Taken together, we have confirmed that this tri-receptor has assembled in a N1-2A-N1-2C arrangement and adopted an asymmetric architecture on NTDs, LBDs and TMD layers (Fig. 4a).

Based on the knowledge that both N1-N2A[22,43] and N1-N2C di-receptors exhibit asymmetric features, it is of interest to note that the N2A and N2C subunits in the tri-receptor share a conformation similar to that of chain B in N1-N2A (PDB 6MMP; ref. [22]) and of chain D in the N1-N2C di-receptors, respectively, as characterized by NTD-LBD angles and extracellular domain superimposition (Fig. 4c). We also stretched the linker conformation from our high-resolution structures of N1-2C di- and N1-2A-2C tri-receptors, and found both N2C linkers in chain D adopted a similar vertical configuration, whereas N2C in chain B of the di-receptors adopted a flattened configuration (Fig. 4d). This asymmetric arrangement was also adopted in the LBD layer. Superimposing the N1-LBDs within the intra- or inter-dimer, we found that N2A-LBD displayed a 4.3° rotation or 4.8° inward rolling relative to the conformation of N2C-LBD (Extended Data Fig. 7d). These findings demonstrate that one protomer conformation of N2A and N2C in the corresponding di-receptors was precisely integrated into the N1-N2A-N2C tri-receptors (Supplementary Video 2).

The PYD-106 insensitivity of the N1-N2A-N2C tri-receptor can thus be attributed to the fact that N2C in the tri-receptor adopts the conformation of chain D in the N1-N2C di-receptor, with R2-D1 lobes spatially disconnected (Extended Data Fig. 9c). The structural

and functional results indicate that the PYD-106 binding depends highly on the conformational specificity of the N2C subunit adopted in di- or tri-receptors. Together, these findings provide structural insight into the distinct biophysical and pharmacological properties of the tri-receptors[40].

Discussion

In this Article we have demonstrated the molecular architecture of N2C- or N2D-containing NMDA receptors and provided structural insights into the subtype-specific gating mechanism and pharmacological properties of these subtypes. To elucidate the molecular determinants for distinct biophysical and pharmacological profiles[1,2], we performed a comprehensive structural analysis of the major NMDA subtypes, including the N1-N2A-N2C tri-receptor and four types of N1-N2 di-receptor in the same Gly-Glu bound state (Fig. 5a). On the NTD layer, from the N2A to N2D di-receptors, individual N2-NTDs adopt a progressively open to close conformation, and the R2-R2 distance within the NTD heterodimer also increases gradually (Fig. 5b). At the tetrameric interface, the distance between two R2 lobes in N2-NTD increases gradually from the N2A to N2D di-receptors (Fig. 5b). These results strongly support the notion that the differential function of the NMDA receptors is controlled by the conformation of N2-NTD[29,30].

To evaluate the subunit cooperativity between the NTD and LBD layers, we noted that the N2A subunits exhibit strong interactions, whereas the N2D subunits display loose contacts, as shown by the distance between the NTD-R2 and LBD-D1 lobes (Fig. 5c). In the structure of N1-N2A-N2B tri-receptors, N2A was also shown to adopt a more extensive NTD-LBD interaction than the N2B subunit[44]. As an exception, chain B of N2C in di-receptors displays the most extensive interaction between R2 and D1 lobes (Fig. 5c, dashed box). This was further evidenced by the asymmetric assembly and unique PYD-106 binding feature in the N2C di-receptors (Fig. 3).

On the LBD layer, neither the individual clamshell of N2 (D1-D2 distance of ~26.5 Å) nor the N1-N2 LBD heterodimer (D2-D2 distance in Fig. 5d) shows a consistent conformational tendency among the four subtypes of di-receptor. With respect to the LBD tetramer, the two N2-LBDs increasingly move away from the N2A to N2D di-receptors. This probably reflects allosteric coupling, with a tendency of increasing separation between the two R2 lobes on the NTD layer (Fig. 5d). Finally, in all the above measured parameters, the individual N2A and N2C subunits in the tri-receptors retain structural features similar to those of the corresponding N2A (chain B) and N2C (chain D) chains in both di-receptors (Fig. 5b–d). Altogether, these findings reveal the molecular structure and functional diversity of NMDA receptors and pave the way for structure-based drug design with subtype specificity.

Online content

Any methods, additional references, Nature Portfolio reporting summaries, source data, extended data, supplementary information, acknowledgements, peer review information; details of author contributions and competing interests; and statements of data and code availability are available at https://doi.org/10.1038/s41594-023-00959-z.

References

1. Traynelis, S. F. et al. Glutamate receptor ion channels: structure, regulation and function. *Pharm. Rev.* **62**, 405–496 (2010).
2. Paoletti, P., Bellone, C. & Zhou, Q. NMDA receptor subunit diversity: impact on receptor properties, synaptic plasticity and disease. *Nat. Rev. Neurosci.* **14**, 383–400 (2013).
3. Zhu, S. & Paoletti, P. Allosteric modulators of NMDA receptors: multiple sites and mechanisms. *Curr. Opin. Pharmacol.* **20**, 14–23 (2015).
4. Stroebel, D. & Paoletti, P. Architecture and function of NMDA receptors: an evolutionary perspective. *J. Physiol.* **599**, 2615–2638 (2021).
5. Monyer, H., Burnashev, N., Laurie, D. J., Sakmann, B. & Seeburg, P. H. Developmental and regional expression in the rat brain and functional properties of four NMDA receptors. *Neuron* **12**, 529–540 (1994).
6. Lu, C. et al. NMDA receptor subtypes at autaptic synapses of cerebellar granule neurons. *J. Neurophysiol.* **96**, 2282–2294 (2006).
7. Ravikrishnan, A. et al. Region-specific expression of NMDA receptor GluN2C subunit in parvalbumin-positive neurons and astrocytes: analysis of GluN2C expression using a novel reporter model. *Neuroscience* **380**, 49–62 (2018).
8. Yamasaki, M. et al. Opposing role of NMDA receptor GluN2B and GluN2D in somatosensory development and maturation. *J. Neurosci.* **34**, 11534–11548 (2014).
9. Mao, Z. et al. NMDA receptors containing GluN2C and GluN2D subunits have opposing roles in modulating neuronal oscillations; potential mechanism for bidirectional feedback. *Brain Res.* **1727**, 146571 (2020).
10. Tsuchida, N. et al. GRIN2D variants in three cases of developmental and epileptic encephalopathy. *Clin. Genet.* **94**, 538–547 (2018).
11. XiangWei, W. et al. Heterogeneous clinical and functional features of GRIN2D-related developmental and epileptic encephalopathy. *Brain* **142**, 3009–3027 (2019).
12. Zhang, X., Feng, Z. J. & Chergui, K. GluN2D-containing NMDA receptors inhibit neurotransmission in the mouse striatum through a cholinergic mechanism: implication for Parkinson's disease. *J. Neurochem.* **129**, 581–590 (2014).
13. Feng, Z. J., Zhang, X. & Chergui, K. Allosteric modulation of NMDA receptors alters neurotransmission in the striatum of a mouse model of Parkinson's disease. *Exp. Neurol.* **255**, 154–160 (2014).
14. Liu, J. et al. Facilitation of GluN2C-containing NMDA receptors in the external globus pallidus increases firing of fast spiking neurons and improves motor function in a hemiparkinsonian mouse model. *Neurobiol. Dis.* **150**, 105254 (2021).
15. Khlestova, E., Johnson, J. W., Krystal, J. H. & Lisman, J. The role of GluN2C-containing NMDA receptors in ketamine's psychotogenic action and in schizophrenia models. *J. Neurosci.* **36**, 11151–11157 (2016).
16. Shelkar, G. P., Gandhi, P. J., Liu, J. & Dravid, S. M. Cocaine preference and neuroadaptations are maintained by astrocytic NMDA receptors in the nucleus accumbens. *Sci. Adv.* **8**, eabo6574 (2022).
17. Salimando, G. J., Hyun, M., Boyt, K. M. & Winder, D. G. BNST GluN2D-containing NMDA receptors influence anxiety- and depressive-like behaviors and modulate cell-specific excitatory/inhibitory synaptic balance. *J. Neurosci.* **40**, 3949–3968 (2020).
18. Karakas, E. & Furukawa, H. Crystal structure of a heterotetrameric NMDA receptor ion channel. *Science* **344**, 992–997 (2014).
19. Lee, C. H. et al. NMDA receptor structures reveal subunit arrangement and pore architecture. *Nature* **511**, 191–197 (2014).
20. Tajima, N. et al. Activation of NMDA receptors and the mechanism of inhibition by ifenprodil. *Nature* **534**, 63–68 (2016).
21. Zhu, S. et al. Mechanism of NMDA receptor inhibition and activation. *Cell* **165**, 704–714 (2016).
22. Jalali-Yazdi, F., Chowdhury, S., Yoshioka, C. & Gouaux, E. Mechanisms for zinc and proton inhibition of the GluN1/GluN2A NMDA receptor. *Cell* **175**, 1520–1532 (2018).
23. Zhang, J. B. et al. Structural basis of the proton sensitivity of human GluN1-GluN2A NMDA receptors. *Cell Rep.* **25**, 3582–3590 (2018).
24. Chou, T. H., Tajima, N., Romero-Hernandez, A. & Furukawa, H. Structural basis of functional transitions in mammalian NMDA receptors. *Cell* **182**, 357–371 (2020).
25. Wang, H. et al. Gating mechanism and a modulatory niche of human GluN1-GluN2A NMDA receptors. *Neuron* **109**, 2443–2456 (2021).

26. Zhang, Y. et al. Structural basis of ketamine action on human NMDA receptors. *Nature* **596**, 301–305 (2021).
27. Regan, M. C. et al. Structural mechanism of functional modulation by gene splicing in NMDA receptors. *Neuron* **98**, 521–529 (2018).
28. Vance, K. M., Hansen, K. B. & Traynelis, S. F. GluN1 splice variant control of GluN1/GluN2D NMDA receptors. *J. Physiol.* **590**, 3857–3875 (2012).
29. Gielen, M., Siegler Retchless, B., Mony, L., Johnson, J. W. & Paoletti, P. Mechanism of differential control of NMDA receptor activity by NR2 subunits. *Nature* **459**, 703–707 (2009).
30. Yuan, H., Hansen, K. B., Vance, K. M., Ogden, K. K. & Traynelis, S. F. Control of NMDA receptor function by the NR2 subunit amino-terminal domain. *J. Neurosci.* **29**, 12045–12058 (2009).
31. Rachline, J., Perin-Dureau, F., Le Goff, A., Neyton, J. & Paoletti, P. The micromolar zinc-binding domain on the NMDA receptor subunit NR2B. *J. Neurosci.* **25**, 308–317 (2005).
32. Sullivan, J. M. et al. Identification of two cysteine residues that are required for redox modulation of the NMDA subtype of glutamate receptor. *Neuron* **13**, 929–936 (1994).
33. Rosenmund, C., Clements, J. D. & Westbrook, G. L. Nonuniform probability of glutamate release at a hippocampal synapse. *Science* **262**, 754–757 (1993).
34. Zhu, S., Stroebel, D., Yao, C. A., Taly, A. & Paoletti, P. Allosteric signaling and dynamics of the clamshell-like NMDA receptor GluN1 N-terminal domain. *Nat. Struct. Mol. Biol.* **20**, 477–485 (2013).
35. Riou, M., Stroebel, D., Edwardson, J. M. & Paoletti, P. An alternating GluN1-2-1-2 subunit arrangement in mature NMDA receptors. *PLoS ONE* **7**, e35134 (2012).
36. Esmenjaud, J. B. et al. An inter-dimer allosteric switch controls NMDA receptor activity. *EMBO J.* **38**, e99894 (2019).
37. Dravid, S. M., Prakash, A. & Traynelis, S. F. Activation of recombinant NR1/NR2C NMDA receptors. *J. Physiol.* **586**, 4425–4439 (2008).
38. Zimmerman, S. S. et al. Design, synthesis and structure-activity relationship of a novel series of GluN2C-selective potentiators. *J. Med. Chem.* **57**, 2334–2356 (2014).
39. Khatri, A. et al. Structural determinants and mechanism of action of a GluN2C-selective NMDA receptor positive allosteric modulator. *Mol. Pharmacol.* **86**, 548–560 (2014).
40. Bhattacharya, S. et al. Triheteromeric GluN1/GluN2A/GluN2C NMDARs with unique single-channel properties are the dominant receptor population in cerebellar granule cells. *Neuron* **99**, 315–328 (2018).
41. Kaiser, T. M. et al. The bioactive protein-ligand conformation of GluN2C-selective positive allosteric modulators bound to the NMDA receptor. *Mol. Pharmacol.* **93**, 141–156 (2018).
42. Cathala, L., Misra, C. & Cull-Candy, S. Developmental profile of the changing properties of NMDA receptors at cerebellar mossy fiber-granule cell synapses. *J. Neurosci.* **20**, 5899–5905 (2000).
43. Jalali-Yazdi, F. & Gouaux, E. NMDA receptors' structural asymmetry. *Microsc. Microanal.* **25**, 1218–1219 (2019).
44. Lu, W., Du, J., Goehring, A. & Gouaux, E. Cryo-EM structures of the triheteromeric NMDA receptor and its allosteric modulation. *Science* **355**, eaal3729 (2017).

Publisher's note Springer Nature remains neutral with regard to jurisdictional claims in published maps and institutional affiliations.

Springer Nature or its licensor (e.g. a society or other partner) holds exclusive rights to this article under a publishing agreement with the author(s) or other rightsholder(s); author self-archiving of the accepted manuscript version of this article is solely governed by the terms of such publishing agreement and applicable law.

© The Author(s), under exclusive licence to Springer Nature America, Inc. 2023

Methods

Plasmid construction

For structural elucidation of the N1-N2D receptors, the complementary DNAs of WT *Homo sapiens GRIN1-1a* (M1-Q847, NM_007327.4) *GRIN1-1b* (M1-Q868, NM_001185090.2) and *GRIN2D* (M1-P879, NM_000836.4) were cloned into pEG-BacMam vector[45]. Strep-tag II was fused to the C terminus of N2D. For biochemistry and electrophysiology, full-length WT *Homo sapiens GRIN1-1a*, *GRIN2D, GRIN2A* (NM_001134407.3), *GRIN2B* (NM_007327.4) were cloned into pCI^{-}neo vector[46], a gift from H. Yuan (Emory University, USA). Chimeric constructs were generated using the Gibson assembling kit (NEBuilder M5520AA). Mutant constructs were obtained by performing site-directed mutagenesis on WT constructs using Takara KOD-FX DNA polymerase.

For structural studies of N2C-containing receptors, WT *Rattus norvegicus GRIN1-1a* (M1-Q847, NP_058706), *GRIN2A* (M1-F841, NP_036705) and *GRIN2C* (M1-V839, NP_036707) followed by a 3C protease cleavage site (LEVLFQGP) were also cloned into pEG-BacMam vectors. For the N1-N2C receptor, a 6×His tag, an mRuby encoding sequence, followed by a Strep-tag II were fused to the C terminus for N1 and N2C, respectively. For the N1-N2A-N2C receptor, a green fluorescent protein (GFP) sequence followed by an affinity tag of 6×His or Strep-tag II was placed at the C terminus of N2A or N2C. The N2A and N2C subunits were subcloned into one vector linked by T2A (EGRGSLLTCGDVEENPGP) self-cleaving peptide.

Protein expression and purification

Recombinant baculovirus was produced using sf9 insect cells following the instructions of the Bac-to-Bac TOPO Expression System (Invitrogen, A11339). Suspended HEK293S GnTI^{-} cells at a concentration of 3.5–4.0 × 10^6 ml^{-1} at 37 °C were infected with P2 virus. At 8–12 h post-infection, 10 μM MK-801 and 10 mM sodium butyrate were co-added into the culture medium to boost protein expression. Cells were transferred to 30 °C for an additional 48–60 h, and then collected by centrifugation at 7,000*g* for 20 min.

The cell pellet was resuspended and sonicated with Tris-buffered saline (TBS; 150 mM NaCl, 20 mM Tris, pH 8.0), solubilized in TBS buffer supplemented with 1% lauryl maltose neopentyl glycol (L-MNG), 2 mM cholesterol hemisuccinate (CHS), a protease inhibitor cocktail of 0.8 μM aprotinin, 2 mM pepstatin A, 2 μg ml^{-1} leupeptin and 1 mM phenylmethyl sulfonyl fluoride (PMSF), 1 mM Gly, 1 mM Glu and 100 μM ethylenediamine tetraacetic acid (EDTA) for 1.5 h at 4 °C. After ultracentrifugation at 40,000*g*, the supernatant was incubated with streptactin resin. The resin was rinsed with wash buffer (TBS supplemented with 0.1% L-MNG, 2 mM CHS, 2 mM Gly, 2 mM Glu and 100 μM EDTA), and eluted with wash buffer supplemented with 5 mM D-desthiobiotin. The eluted protein was concentrated and further injected into a Superose 6 Increase column (GE Healthcare) for size-exclusion chromatography (SEC) in TBS buffer supplemented with 0.1% digitonin, 5 μM CHS, 0.1 mM CHAPSO, 1 mM Gly, 1 mM Glu and 100 μM EDTA. The peak fraction was pooled and concentrated to ~4 mg ml^{-1} for cryo-EM grid preparation.

For the N1-N2A-N2C tri-receptor, 5 mM imidazole was added to the elution from streptactin affinity chromatography, and the sample was bound to immobilized metal affinity chromatography nickel resin for His-tag purification. The nickel resin was rinsed with wash buffer supplemented with 15 mM imidazole, and the tri-receptor protein was eluted using wash buffer supplemented with 250 mM imidazole. Next, 400 μM (*R*/*S*)-PYD-106 (Aobious, AOB6695) was added into N1-N2C protein for the PYD-106 bound structure, and 1 mM Gly and 600 μM (*R*/*S*)-CPP (Sigma, C104-25MG) were added into N1a-N2D protein for the Gly-CPP bound structure. All purification procedures were conducted at 4 °C.

Cryo-EM sample preparation, data acquisition and processing

A 3-μl volume of protein sample was applied to a glow-discharged 300 mesh Quantifoil R1.2/1.3 (Au) grid (Electron Microscopy China, BQR1.2/1.3-3A) using a FEI Vitrobot system (Thermo Fisher), with the chamber environment controlled at 8 °C and 100% humidity. Grids were blotted for 3 s and immediately plunged into liquid ethane for vitrification.

Cryo-EM data were collected on a 300-kV Titan Krios G3 electron microscope (FEI) equipped with a K3 Summit direct electron detector (Gatan) and GIF quantum energy filter. The pixel size in the super-resolution counting mode was set to 0.5355 Å for all datasets of N2C-containing receptors and to 0.415, 0.5335 and 0.5355 Å for the different datasets of N2D-containing receptors. Each movie stack was dose-fractionated over 40–50 frames with a total dose of 60 electrons. The defocus values of the movie stacks varied between −1.2 μm and −2.5 μm. Automatic data collection was conducted using Serial EM 3.7.11.

Beam-induced motion and drift correction were performed using MotionCor2 1.4.0[47]. CTF parameters for each micrograph were determined by Gctf_v1.06[48]. Approximately 2,000 particles were manually picked and subjected to an initial reference-free 2D classification. Auto-picked particles were extracted and then subjected to several rounds of reference-free 2D classification and 3D classification. For N2C-containing receptors, no symmetry was applied during the data-processing. For N1-N2D receptors, *C*2 symmetry was applied for the 3D refinement procedure. In addition, TMD-focus 3D classification on N1-N2D receptors in the Gly-Glu bound state did not improve the overall density of the TMD region. The 'gold-standard' Fourier shell correlation (FSC) resolution were calculated with a soft shape mask applied to independent unfiltered half maps, with 0.143 criterion[49]. Data processing was mainly conducted with Relion 3.1.1[50], except for 3D classification and 3D refinement in the datasets of the Gly-Glu and Gly-CPP bound N1-N2D receptors, which were conducted with CryoSPARC 3.0[51]. More detailed information about data collection and processing is provided in Extended Data Figs. 1, 4, 5 and 7 and Tables 1 and 2.

Model building and refinement

Initial templates of the N1a-N2D, N1b-N2D, N1-N2C di-receptors and N1-N2A-N2C tri-receptor were generated with SWISS-MODEL[52] (https://swissmodel.expasy.org/), based on homology structures of the N1b-N2B receptor (PDB 6WI1; ref. [24]) and N1a-N2A receptor (PDB 6MMT; ref. [22]), respectively. Each structural coordinate was optimized by Hermite® Platform (https://hermite.dp.tech, DP Technology). Rigid-body docking with ChimeraX 1.14[53] was used to fit the structural coordinates into the density maps. Flexible fitting was done with molecular dynamics flexible fitting (MDFF)[54] simulations with the CHARMM36m force field[55]. The simulation temperature was maintained at 300 K using the Langevin algorithm[56], and the generalized Born implicit solvent model[57,58] was used to describe the solvation effects. The models were then subjected to iterative manual adjustment in Coot 0.9.6.1[59] and real-space refinement in Phenix 1.20.1[60]. The local resolution of density maps was estimated using ResMap-1.1.4[61].

Two-electrode voltage-clamp recording

Xenopus oocytes were prepared, injected and voltage-clamped as previously reported[25]. TEVC recording was performed in extracellular solution containing 100 mM NaCl, 2.5 mM KCl, 0.3 mM $BaCl_2$, 5 mM HEPES, 0.01 mM diethylenetriamine penta-acetic acid, pH adjusted to 7.3 with NaOH. The maximum current of the NMDA receptors was induced by co-application of 100 μM Gly and 100 μM Glu, at a holding potential of −60 mV. Current responses were recorded by Clampex 10.6 (Molecular Devices) software. In the DTT reduction experiment, oocytes were incubated for 15 min in solution containing 5 mM DTT, 88 mM NaCl, 10 mM HEPES, 1 mM KCl, 2.4 mM $NaHCO_3$, 0.33 mM $Ca(NO_3)_2$, 0.41 mM $CaCl_2$ and 0.82 mM $MgSO_4$, pH adjusted to 7.6 with NaOH.

To evaluate the relative Po, 200 nM MK-801 (Abcam, ab120027) was applied upon the maximum activation of the NMDA receptors.

MK-801 inhibition constants (τ_{on}) were calculated by fitting the current response trace in the inhibition phase (between 10% and 90% of the maximal inhibition) with a single-exponential fit. Each value of mutant receptors was normalized to the mean τ_{on} of the WT N1-N2D receptors.

Reconstitution of proteoliposomes

Membrane protein was reconstituted into artificial liposomes as previously described[62]. Asolectin (Sigma-Aldrich, 11145-50G) was dissolved in chloroform at a stock concentration of 25 mg ml^{-1} and dried under a liquid-nitrogen stream to form a thin layer along the inner wall of the glass tube. Subsequently, 1 ml of 0.4 M sucrose was added and the tube was incubated at 50 °C in a water bath for 3 h until a lipid cloud was formed. Purified CTD-truncated N1^{E698C}-N2D receptor protein was then added at a weight ratio of protein to lipid of 1:1,000, and further incubated for 3 h at 4 °C with a shaking speed at 100 r.p.m. Freshly reconstituted proteoliposomes were mixed with bath buffer containing 140 mM NaCl, 2.8 mM KCl, 0.5 mM $CaCl_2$, 10 mM HEPES and 0.01 mM 1,2-bis(*o*-aminophenoxy)ethane-*N*,*N*,*N*′,*N*′-tetraacetic acid, pH adjusted to 7.3 with NaOH, and used for single-channel recording experiment.

Single-channel recording

Single-channel recording was performed using pipette buffer containing 140 mM CsCl, 5 mM EGTA, 0.1 mM Gly, 1 mM Glu and 10 mM HEPES, pH adjusted to 7.2 with CsOH, and the abovementioned bath buffer. Borosilicate glass pipettes (BF150-86-10, Sutter Instrument) were fabricated using a P-97 puller (Sutter Instrument) with resistance in the range of 3–6 MΩ. The patch resistance increased to a gigaohm seal (>1 GΩ) after the pipette formed a tight seal with the liposome membrane, then single-channel currents were recorded with cell-attached patches at a holding potential of +20 mV and the data were collected with an EPC-10 amplifier and Pulse software Patchmaster v2x90.3 (HEKA Electronic) with a 0.5-kHz low-pass filter and 50-Hz notch filter. A 10-s duration from independent recordings was selected for data analysis.

Western blotting

The WT and mutant N1-N2D receptors were expressed in HEK293S cells by polyethylenimine transfection (at a ratio of 1:3 of DNA and polyethylenimine). Cells were collected and solubilized in lysis buffer (20 mM Tris pH 8.0, 150 mM NaCl, 1% L-MNG, 0.8 μM aprotinin, 2 mM pepstatin A, 2 μg ml^{-1} leupeptin and 1 mM PMSF) for 1 h. Samples of N1-N2D or purified N1-N2A-N2C protein were subjected to loading buffer in the presence or absence of 0.5 M DTT and separated on sodium dodecyl sulfate (SDS) polyacrylamide gel electrophoresis (4–6%). The protein was transferred to polyvinylidene fluoride membranes and immunoblotted with monoclonal antibodies (anti-N1, Millipore, MAB1586, 1:1,000 dilution; anti-N2D, Millipore, MAB5578, 1:500 dilution; anti-strep, Abcam, ab252885, 1:1,000 dilution; anti-6×his, Abcam, ab15149, 1:1,000 dilution) and subsequently with secondary antibodies of horseradish peroxidase-conjugated (mouse immunoglobulin G, Cell Signaling Technology, 7076s, 1:4,000 dilution; rabbit immunoglobulin G, Cell Signaling Technology, 7074P2, 1:4,000 dilution). Protein bands were visualized by ECL substrate (Tanon, #180-501).

Molecular dynamics simulation

An atomistic system of N1-N2A (PDB 7EU7[26]), N1-N2D and N1-N2C (both symmetric and asymmetric structures) embedded in a 1-palmitoyl-2-oleoyl-*sn*-glycero-3-phosphocholine (POPC) bilayer was set up with CHARMM-GUI[63]. One copy of the protein and 771 POPC molecules were placed in a cubic simulation box. The system was solvated in 0.15 M NaCl solution, making a total of 597,467 atoms. Simulations were performed using GROMACS[64] version 2021.3 with the CHARMM36 force field[65] and TIP3P water model[66]. The system was equilibrated in six steps with gradually decreasing restraining force constants on the protein. Two repeats of 200 ns of unrestrained atomistic simulations were then performed. The particle mesh Ewald (PME) method[67] was used to model the long-range electrostatics (<1 nm). Temperature coupling was done with a V-rescale thermostat[68] at 310 K. a Parrinello–Rahman barostat[69] with a reference pressure of 1 bar and a compressibility of 4.5×10^{-5} bar was applied for pressure control. Covalent bonds were constrained to their equilibrium length by the LINCS algorithm[70]. The integration steps of all simulations were set to 2 fs.

Mass spectrometry analysis

A 20-μg sample of the protein of the N1-N2C or N1-N2A-N2C receptors was buffer-exchanged into denaturing buffer with 8 M urea and 50 mM NH_4HCO_3, pH 8.0. Samples were reduced and alkylated by tris(2-carboxyethyl) phosphine and iodoacetamide, and exchanged into digestion buffer (10 mM NH_4HCO_3, pH 8.0) and digested by Lys-C at 37 °C for 1 h. Then, trypsin, Glu-C or chymotrypsin was added, respectively, and further digested overnight. The supernatant was collected and acidified by 10% formic acid (FA) to pH 2.0 and subjected to lyophilization then stored at −20 °C until use.

The peptides were resuspended in 0.1% FA, and 400 ng was injected for LC-MS/MS analysis. The peptides were first loaded onto a C18 trap column (3 μm, 120 Å) with buffer A (0.1% FA in H_2O) and then separated with a C18 analytical column (2.4 μm, 120 Å) by gradient elution of 5–35% buffer B (0.1% FA in acetonitrile) in 65 min. MS data were collected by a Thermo Fusion Lumos mass spectrometer (Thermo Fisher Scientific) in a data-dependent acquisition manner. The full MS spectra were obtained by an Orbitrap analyzer with a resolution of 120,000 and a scan range of 350–1,800 *m*/*z*. Precursor ions with a charge state of 2+ to 8+ and a minimum intensity of 5×10^4 were isolated and subjected to high-energy collisional dissociation (HCD) with a normalized energy of 28% and electron-transfer/high-energy collision dissociation (EThcD). Calibrated charge-dependent ETD parameters were used, and the supplemental activation collision energy was set at 15%. MS2 data, including HCD and EThcD, were obtained by the Orbitrap analyzer with a resolution of 30,000.

The MS data were all processed by pGlyco 3.0[71]. Protein sequences of the sample were used as a database for peptide searching. The max miss cleavage was set to 3. The mass tolerances of MS1 and MS2 were set to 10 ppm and 20 ppm, respectively. The results were further analyzed and visualized using R with 'data.table', 'tidyverse' and 'ggsci' packages.

Structural analysis

For the structural measurements, the NTD and LBD were separated into R1 and R2, and D1 and D2 lobes, respectively. The COM of each domain or lobe was calculated in PyMOL 2.5.2 using the 'center_of_mass' script. NTD-LBD vector angles were calculated in PyMOL using the 'vector_angle' script, with one vector connecting the COMs of the NTD-R2 and NTD-R1 lobes, and the other vector connecting the COMs of the LBD-D1 and LBD-D2 lobes. Rotation between the domains was calculated using the 'draw_rotation_axis' script in PyMOL. The dimensions of the receptors were obtained by running the 'draw_protein_dimensions' script in PyMOL. The open–closed dihedral angles of NTD were measured by connecting the Cα atoms of E102, E147, T278, E232 for N2C; E107, Q152, Y281, E235 for N2A; P124, E169, S309, E252 for N2D; and H101, H146, L271, D226 for N1a. The twisted–untwisted dihedral angles of NTD were measured by connecting the Cα atoms of I129, A325, E399 and F257 for N2D; M112, G297, E373, L240 for N2A; and V107, V287, G365, Y232 for N1a. The open–closed dihedral angles of LBD were measured by connecting the Cα atoms of I403, S688, V735, A715 for N1a; I424, S709, V756, A736 for N1b; and P124, E525, S309, E169 for N2D, respectively.

Data analysis, statistics and reproducibility

For single-channel recording, Pulse files were converted into PCLAMP format using ABF File Utility, version 2.1.75 (Synaptosoft). The current traces of both single-channel and TEVC recording were analyzed and

fitted by Clampfit 10.7 (Axon Instruments). GraphPad Prism 8.0 software (Graphpad Software) was used for statistical analysis and graph generation. All histograms were fitted by a sum of Gaussians.

Protein expression and purification for cryo-EM sample preparation were reproduced at least three times independently. For gel electrophoresis analysis and western blot, multiple batches (repeated at least three times) of experiments were performed to ensure reproducibility. At least three repeats on independent oocytes in the TEVC recording and six repeats on independent patches in the single-channel recording were performed, and showed consistent results.

Reporting summary

Further information on research design is available in the Nature Portfolio Reporting Summary linked to this Article.

Data availability

Cryo-EM density maps and structural coordinates have been deposited in the Electron Microscopy Database and Protein Data Bank under accession codes EMD-33792 and PDB 7YFL for Gly-Glu bound N1a-N2D, EMD-33788 and PDB 7YFF for Gly-CPP bound N1a-N2D, EMD-33795 and PDB 7YFO for crosslinked N1a^{E698C}-N2D, EMD-33798 and PDB 7YFR for non-crosslinked N1a^{E698C}-N2D, EMD-33793 and PDB 7YFM for Gly-Glu bound N1b-N2D, EMD-33789 and PDB 7YFG for Gly-Glu bound N1a-N2C in the asymmetric conformation, EMD-34674 and PDB 8HDK for Gly-Glu bound N1a-N2C in the symmetric conformation, EMD-33790 and PDB 7YFH for PYD-106 bound N1a-GluN2C, and EMD-33791 and PDB 7YFI for Gly-Glu bound N1a-N2A-N2C receptors, respectively. Additional data that support the findings of this study are available from the corresponding author upon request. Source data are provided with this paper.

References

45. Goehring, A. et al. Screening and large-scale expression of membrane proteins in mammalian cells for structural studies. *Nat. Protoc.* **9**, 2574–2585 (2014).
46. Li, D. et al. GRIN2D recurrent de novo dominant mutation causes a severe epileptic encephalopathy treatable with NMDA receptor channel blockers. *Am. J. Hum. Genet.* **99**, 802–816 (2016).
47. Zheng, S. Q. et al. MotionCor2: anisotropic correction of beam-induced motion for improved cryo-electron microscopy. *Nat. Methods* **14**, 331–332 (2017).
48. Zhang, K. Gctf: real-time CTF determination and correction. *J. Struct. Biol.* **193**, 1–12 (2016).
49. Scheres, S. H. RELION: implementation of a Bayesian approach to cryo-EM structure determination. *J. Struct. Biol.* **180**, 519–530 (2012).
50. Fernandez-Leiro, R. & Scheres, S. H. W. A pipeline approach to single-particle processing in RELION. *Acta Crystallogr. D Struct. Biol.* **73**, 496–502 (2017).
51. Punjani, A., Rubinstein, J. L., Fleet, D. J. & Brubaker, M. A. cryoSPARC: algorithms for rapid unsupervised cryo-EM structure determination. *Nat. Methods* **14**, 290–296 (2017).
52. Arnold, K., Bordoli, L., Kopp, J. & Schwede, T. The SWISS-MODEL workspace: a web-based environment for protein structure homology modelling. *Bioinformatics* **22**, 195–201 (2006).
53. Pettersen, E. F. et al. UCSF ChimeraX: structure visualization for researchers, educators and developers. *Protein Sci.* **30**, 70–82 (2021).
54. Trabuco, L. G., Villa, E., Mitra, K., Frank, J. & Schulten, K. Flexible fitting of atomic structures into electron microscopy maps using molecular dynamics. *Structure* **16**, 673–683 (2008).
55. Huang, J. et al. CHARMM36m: an improved force field for folded and intrinsically disordered proteins. *Nat. Methods* **14**, 71–73 (2017).
56. Allen, M. P. & Tildesley, D. J. *Computer Simulation of Liquids* 2nd edn (Oxford Univ. Press, 2017); https://doi.org/10.1093/oso/9780198803195.001.0001
57. Ghosh, A., Rapp, C. S. & Friesner, R. A. Generalized Born model based on a surface integral formulation. *J. Phys. Chem. B* **102**, 10983–10990 (1998).
58. Tsui, V. C. & Case, D. A. Molecular dynamics simulations of nucleic acids with a generalized Born solvation model. *J. Am. Chem. Soc.* **122**, 2489–2498 (2000).
59. Emsley, P. & Cowtan, K. Coot: model-building tools for molecular graphics. *Acta Crystallogr. D Biol. Crystallogr.* **60**, 2126–2132 (2004).
60. Afonine, P. V. et al. Real-space refinement in PHENIX for cryo-EM and crystallography. *Acta Crystallogr. D Struct. Biol.* **74**, 531–544 (2018).
61. Kucukelbir, A., Sigworth, F. J. & Tagare, H. D. Quantifying the local resolution of cryo-EM density maps. *Nat. Methods* **11**, 63–65 (2014).
62. Battle, A. R., Petrov, E., Pal, P. & Martinac, B. Rapid and improved reconstitution of bacterial mechanosensitive ion channel proteins MscS and MscL into liposomes using a modified sucrose method. *FEBS Lett.* **583**, 407–412 (2009).
63. Jo, S., Kim, T., Iyer, V. G. & Im, W. CHARMM-GUI: a web-based graphical user interface for CHARMM. *J. Comput. Chem.* **29**, 1859–1865 (2008).
64. Abraham, M. J. et al. GROMACS: high performance molecular simulations through multi-level parallelism from laptops to supercomputers. *SoftwareX* **1–2**, 19–25 (2015).
65. Lee, J. et al. CHARMM-GUI input generator for NAMD, GROMACS, AMBER, OpenMM and CHARMM/OpenMM simulations using the CHARMM36 additive force field. *J. Chem. Theory Comput.* **12**, 405–413 (2016).
66. Jorgensen W, C. J. & Madura, J. Comparison of simple potential functions for simulating liquid water. *J. Chem. Phys.* **79**, 926–935 (1983).
67. Essmann, U. et al. A smooth particle mesh Ewald method. *J. Chem. Phys.* **103**, 8577–8593 (1995).
68. Bussi, G., Donadio, D. & Parrinello, M. Canonical sampling through velocity rescaling. *J. Chem. Phys.* **126**, 014101 (2007).
69. Parrinello, M. & Rahman, A. Polymorphic transitions in single crystals: a new molecular dynamics method. *J. Appl. Phys.* **52**, 7182–7190 (1981).
70. Hess, B., Bekker, H., Berendsen, H. J. C. C. & Fraaije, J. G. E. M. E. M. LINCS: a linear constraint solver for molecular simulations. *J. Comput. Chem.* **18**, 1463–1472 (1997).
71. Zeng, W. F., Cao, W. Q., Liu, M. Q., He, S. M. & Yang, P. Y. Precise, fast and comprehensive analysis of intact glycopeptides and modified glycans with pGlyco3. *Nat. Methods* **18**, 1515–1523 (2021).

Acknowledgements

We thank Y. Kong and L. Pan at the Electron Microscopy Facilities of the Center for Excellence in Brain Science and Technology, Chinese Academy of Sciences for assistance with sample screen. We thank B. Zhu and X. Li at the Center for Biological Imaging (CBI), Institute of Biophysics, Chinese Academy of Sciences, Q. Wang and Y. Zhou at the Electron Microscopy Facility, Shanghai Institute of Materia Medica (SIMM), Chinese Academy of Sciences, and Q. Sun and Y. Wang at the Bio-Electron Microscopy Facility, ShanghaiTech University for their help in cryo-EM data collection. We thank Y. Jia at Fudan University for assistance with single-channel recordings. We acknowledge the technological support of the biological mass spectrometry station of Dalian Coherent Light Source. We are grateful to M. Poo for proofreading. We gratefully acknowledge financial support from the STI2030-Major Project (2022ZD0212700), the National Natural

Science Foundation of China (32221003), the Lingang Laboratory (LG 202106-02), the Strategic Priority Research Program of Chinese Academy of Science (XDBS01020000), the Shanghai Municipal Science and Technology Major Project (2018SHZDZX05) and the CAS Youth Interdisciplinary Team to S.Z.

Author contributions

J.Z. and M.Z. purified and froze the protein, collected and analyzed the cryo-EM data, built atomic models and conducted electrophysiology of the N2D and N2C receptors, respectively. H.W., Q.W. and Y.W. carried out in silico calculations. Z.L. and F.W. performed mass spectrometry. N.S. and Z.K. performed biochemistry assays. F.Y. carried out single-channel recordings. Y.L. and F.G. participated in data collection of N2C receptors, respectively. J.Z., M.Z. and S.Z. wrote the manuscript. S.Z. conceived the project and supervised the research.

Competing interests

The authors declare no competing interests.

Additional information

Extended data is available for this paper at https://doi.org/10.1038/s41594-023-00959-z.

Supplementary information The online version contains supplementary material available at https://doi.org/10.1038/s41594-023-00959-z.

Correspondence and requests for materials should be addressed to Shujia Zhu.

Peer review information *Nature Structural & Molecular Biology* thanks Albert Lau, Lonnie P Wollmuth and the other, anonymous, reviewer(s) for their contribution to the peer review of this work. Primary Handling Editor: Katarzyna Ciazynska, in collaboration with the *Nature Structural & Molecular Biology* team. Peer reviewer reports are available.

Reprints and permissions information is available at www.nature.com/reprints.

https://doi.org/10.1038/s41594-023-00959-z

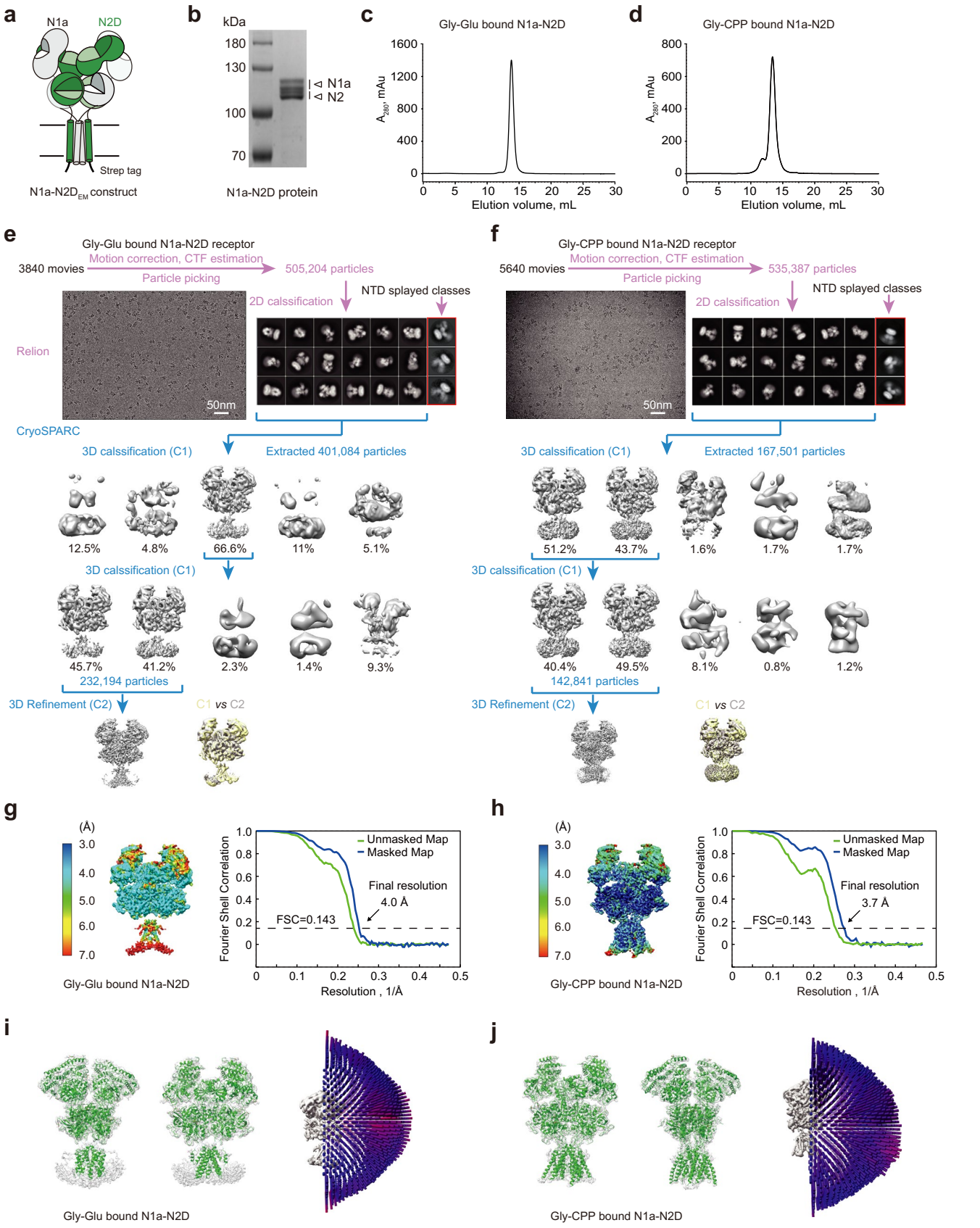

Extended Data Fig. 1 | See next page for caption.

https://doi.org/10.1038/s41594-023-00959-z

Extended Data Fig. 1 | Protein purification and cryo-EM analysis of Gly-Glu and Gly-CPP bound N1a-N2D receptors. a, Schematic illustration of CTD-truncated receptor composed of human N1a (in grey) and strep tag fused N2D (in green) subunits. **b-d**, Coomassie blue gel staining (**b**) and fluorescence SEC (FSEC) analysis of purified Gly-Glu (**c**) and Gly-CPP (**d**) bound N1a-N2D receptors protein. Gel and FSEC analysis were repeated three times. **e, f**, Cryo-EM data-processing workflow of the Gly-Glu (**e**) and Gly-CPP (**f**) bound N1a-N2D receptors. Representative micrographs and 2D average classes are shown. Note that the special 2D averaged class with splayed extracellular domains (highlighted by a red box) was found in both datasets. For both datasets, motion correction, CTF estimation, particle picking and 2D classification were carried out by Relion 3.1.1[50]. Then, 3D classification and 3D refinement were subsequently performed by CryoSPARC[51]. **g, h**, Local resolution representation of density map and Fourier shell correlation (FSC) of Gly-Glu (**g**) and Gly-CPP (**h**) bound N1a-N2D receptor structures. Maps are colored based on the local resolution estimation by ResMap-1.1.4[61]. Masked (blue) and unmasked (green) FSCs of corresponding maps are both shown, where gold standard FSC = 0.143 was applied for the indication of final resolution (dashed line). **i, j**, Representation of model fit to map (left two panels) and the angular distribution of particles used in the final reconstruction (right panel).

https://doi.org/10.1038/s41594-023-00959-z

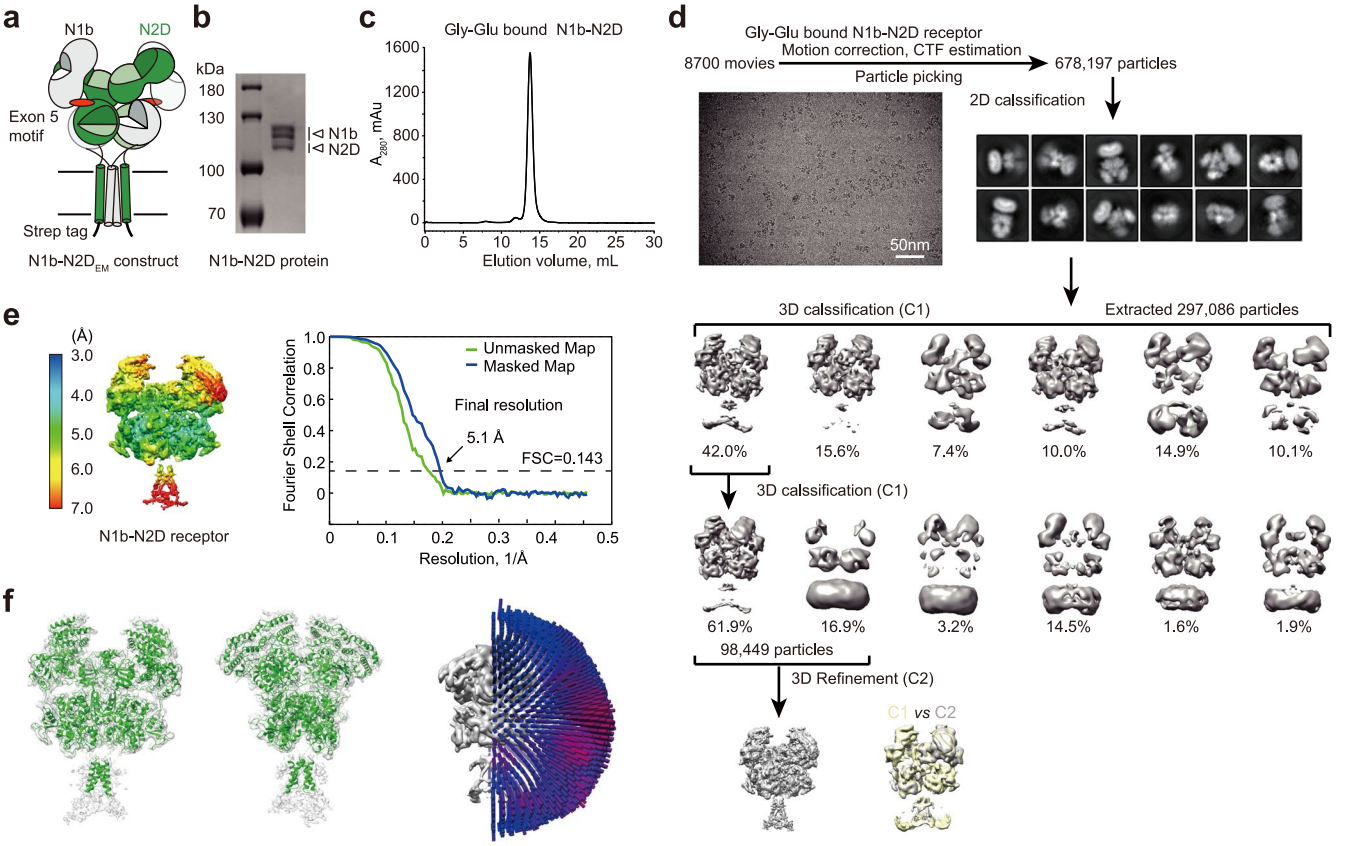

Extended Data Fig. 2 | Protein purification and cryo-EM analysis of N1b-N2D receptors. a, Schematic illustration of CTD-truncated receptor composed of human N1b (in grey) and strep tag fused N2D (in green) subunits. **b**,**c**, Coomassie blue gel staining and FSEC analysis (repeated three times) of purified proteins of N1b-N2D receptors. **d**, Cryo-EM data-processing workflow of N1b-N2D receptor datasets processed by Relion 3.1.1[50]. Representative micrographs, 2D average classes, 3D classes and final density maps are shown. **e**, Local resolution representation of density map and Fourier shell correlation (FSC) of Gly-Glu bound N1b-N2D receptor. Maps are colored based on the local resolution estimation by ResMap-1.1.4[61]. Masked (blue) and unmasked (green) FSCs of corresponding maps are both shown, with gold standard FSC of 0.143 criteria indicated. **f**, Representation of model fit to map (left two panels) and the angular distribution of particles used in the final reconstruction (right panel).

https://doi.org/10.1038/s41594-023-00959-z

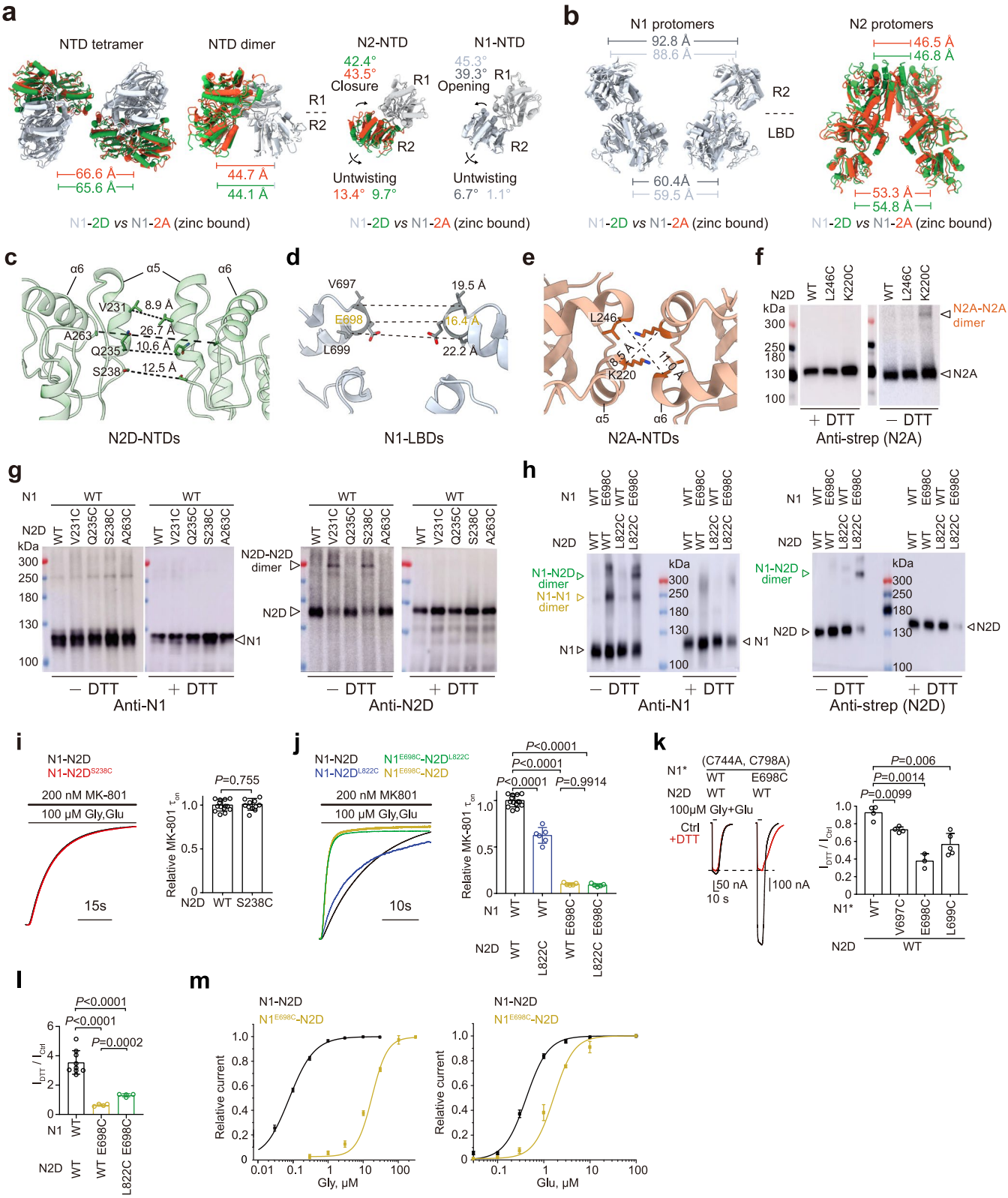

Extended Data Fig. 3 | See next page for caption.

https://doi.org/10.1038/s41594-023-00959-z

Extended Data Fig. 3 | Structural, biochemical and electrophysiological analysis of N1a-N2D receptors. a,**b**, Conformation comparison of NTDs (**a**) and protomers (**b**) between Gly-Glu bound N1-N2D and zinc-bound N1-N2A (PDB:6MMK, ref. [22]) di-receptors. Lines, angles and arrows are illustrated as in Fig. 2 legend. **c**-**e**, Cartoon representation of the tetrameric interface formed by two N2D-NTDs (**c**) and two N1-LBDs (**d**) in Gly-Glu bound N1-N2D receptor, and formed by two N2A-NTDs (**d**) in Gly-Glu bound N1-N2A receptor (PDB:6MMP, ref. [22]), with residues shown in sticks and Cα-Cα distances indicated. **f**-**h**, Western blotting analysis on WT and cysteine-substituted N1-N2A (**f**) and N1-N2D (**g**, **h**) receptors (repeated three times). Bands of N1 and N2 momomers, N1-N2 and N2-N2 dimers are indicated. **i**-**j**, Representative recording traces and relative MK-801 inhibition on-rate kinetics constants (τ_{on}, monoexponential fits) of WT N1-N2D (1.00 ± 0.07, n = 15), N1-N2D^{S238C}(1.01 ± 0.07, n = 12, in **i**), N1-N2D^{L822C} (0.62 ± 0.08, n = 6, in **j**), N1^{E698C}-N2D (0.10 ± 0.01, n = 5, in **j**) and N1^{E698C}-N2D^{L822C} (0.09 ± 0.01, n = 5, in **j**) receptors. **k**,**l**, DTT induced current amplitude changes on WT and mutant receptors. Relative currents (after and before DTT treatment) values, from left to right, are 0.91 ± 0.08 (n = 4), 0.73 ± 0.03 (n = 4), 0.38 ± 0.08 (n = 3) and 0.57 ± 0.13 (n = 5) in **k**, and 3.56 ± 0.80 (n = 9), 0.65 ± 0.07 (n = 4) and 1.33 ± 0.10 (n = 4) in **l**. N1* implies the mutant N1$^{C744A, C798A}$ subunit. **m**, Dose-response curves (fitted by Hill equation) of glycine and glutamate on N1-N2D (Gly EC_{50} of 0.08 ± 0.01 μM, n^H = 1.2 and Glu EC_{50} of 0.42 ± 0.04 μM, n^H = 1.8) and N1^{E698C}-N2D (Gly EC_{50} of 17.49 ± 0.26 μM, n^H = 2 and Glu EC_{50} of 1.66 ± 0.05 μM, n^H = 1.7) receptors. n = 4 oocytes for each group. All data are shown with mean ± SD. For the statistical analysis, *P* values are determined by two-tailed unpaired Student's *t*-test for (**i**) and by one-way ANOVA followed by the Tukey's multiple comparison test for (**j**-**l**).

https://doi.org/10.1038/s41594-023-00959-z

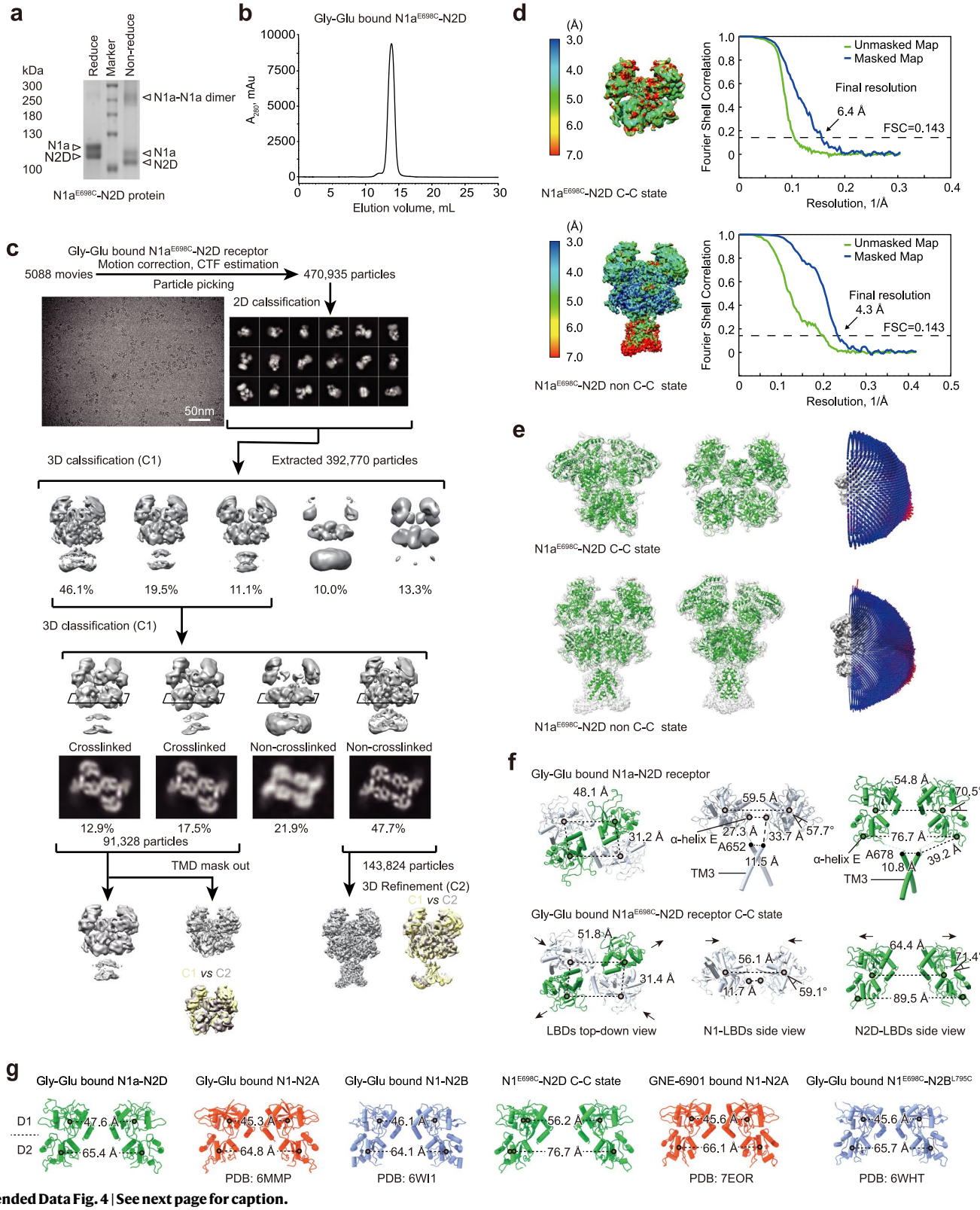

Extended Data Fig. 4 | See next page for caption.

https://doi.org/10.1038/s41594-023-00959-z

Extended Data Fig. 4 | Protein purification, cryo-EM and structural analysis of N1a^{E698C}-N2D receptors. a-b, Coomassie blue gel staining and FSEC analysis (repeated three times) of purified proteins of N1a^{E698C}-N2D receptors. Bands of N1 and N2D monomer and N1-N1 dimer are indicated. **c**, Cryo-EM data-processing workflow of N1b-N2D receptor datasets processed by Relion 3.1.1[50]. Representative micrographs, 2D average classes, 3D classes and final density maps are shown. **d**, Local resolution representation of density map and Fourier shell correlation (FSC) of Gly-Glu bound N1b-N2D receptor. Maps are colored based on the local resolution estimation by ResMap-1.1.4[61]. Masked (blue) and unmasked (green) FSCs of corresponding maps are both shown, with gold standard FSC of 0.143 criteria indicated. **e**, Representation of model fit to map (left four panels) and the angular distribution of particles used in the final reconstruction (right two panels). **f**, Structural analysis of top-down viewed tetrameric LBD (left), of side-viewed two N1 (middle) and N2D (right) protomers. Center-of-mass (COM) of each lobe, domain and α-helix E (P670-R673 for N1 and R696-Q699 for N2D) is shown in empty circle. Cα atoms of N1 A652 and N2D A678 in gate are marked in filled circle. The dihedral angles for indicating opening-closure degree of LBD are assessed by connecting the Cα of I403, S688, V735, A715 in N1, and P124, E525, S309, E169 in N2D, respectively. Arrows indicate the conformational changes of Gly-Glu bound N1^{E698C}-2D C-C state compared to the Gly-Glu bound WT receptor. **g**, Conformational comparison of N2-LBDs in Gly-Glu bound N1a-N2D, Gly-Glu bound N1a^{E698C}-N2D, Gly-Glu bound N1-N2A (PDB:6MMP, ref. [22]), Gly-Glu & GNE-6901 bound N1^{E698C}-N2A^{L794C} (PDB:7EOR, ref. [25]), Gly-Glu bound WT N1b-N2B (PDB:6WI1, ref. [24]), Gly-Glu bound N1b^{E698C}-N2B^{L795C} (PDB:6WHT, ref. [24]) receptors. Dash lines indicate COM distances of D1-D1 and D2-D2 lobes.

https://doi.org/10.1038/s41594-023-00959-z

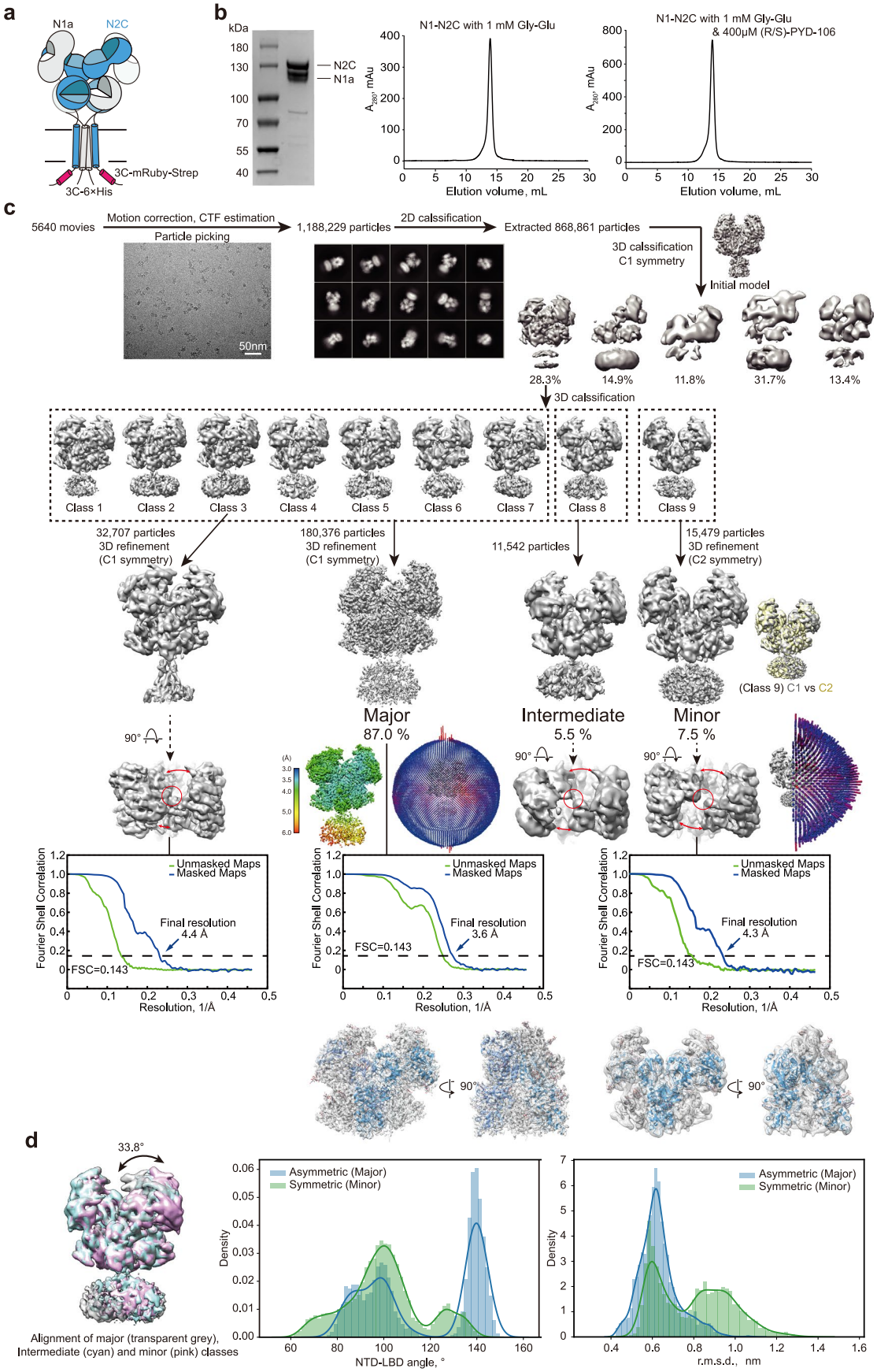

Extended Data Fig. 5 | See next page for caption.

https://doi.org/10.1038/s41594-023-00959-z

Extended Data Fig. 5 | Biochemical analysis and Cryo-EM data processing of N1-N2C di-receptors in Gly-Glu bound state. a, Cartoon representation of N1-N2C receptor, with mRuby-Strep Tag II and 6×His tag placed at the C terminus of N2C and N1 constructs, respectively. **b**, Coomassie blue gel staining of purified protein of N1-N2C receptors (left panel). FSEC profiles of Gly-Glu bound and Gly-Glu & PYD-106 co-bound N1-N2C receptors (right panel). Gel and FSEC analysis were repeated three times. **c**, Cryo-EM data-processing flowchart of N1-N2C receptors in complex with Gly-Glu. Representative micrographs, 2D class average images and 3D classification maps are shown. Class 3 of best TMD signal was processed individually to get a map displaying certain signal of TMD. Proportion of particle quantity and NTD top-down view comparison of the asymmetric major, intermediate and symmetric minor classes are shown. Representation of model fit to map, the angular distribution of particles used in the final reconstruction are shown. Masked (blue) and unmasked (green) FSCs of corresponding maps are both shown, with gold standard FSC of 0.143 criteria indicated. Masked (blue) and unmasked (green) FSCs of corresponding maps are both shown, with gold standard FSC of 0.143 criteria indicated. **d**, Map alignment of asymmetric major (represented by class 3), intermediate (class 8) and minor (class 9) classes. The rotation angle of one NTD heterodimer is indicated. Middle and right panels show the results of three repeats of 200 ns each unrestrained atomistic simulations on both symmetrical and asymmetrical N1A-N2C structures. The histogram and corresponding kernel density estimation are shown. Middle panel shows the NTD-LBD angles of N2C subunits measured throughout the simulations. Right panel shows r.m.s.d. of the least square fitting to the C-alpha atoms, and the first 50 ns of simulations in each repeat were excluded for r.m.s.d. calculation to allow models to fully relax.

https://doi.org/10.1038/s41594-023-00959-z

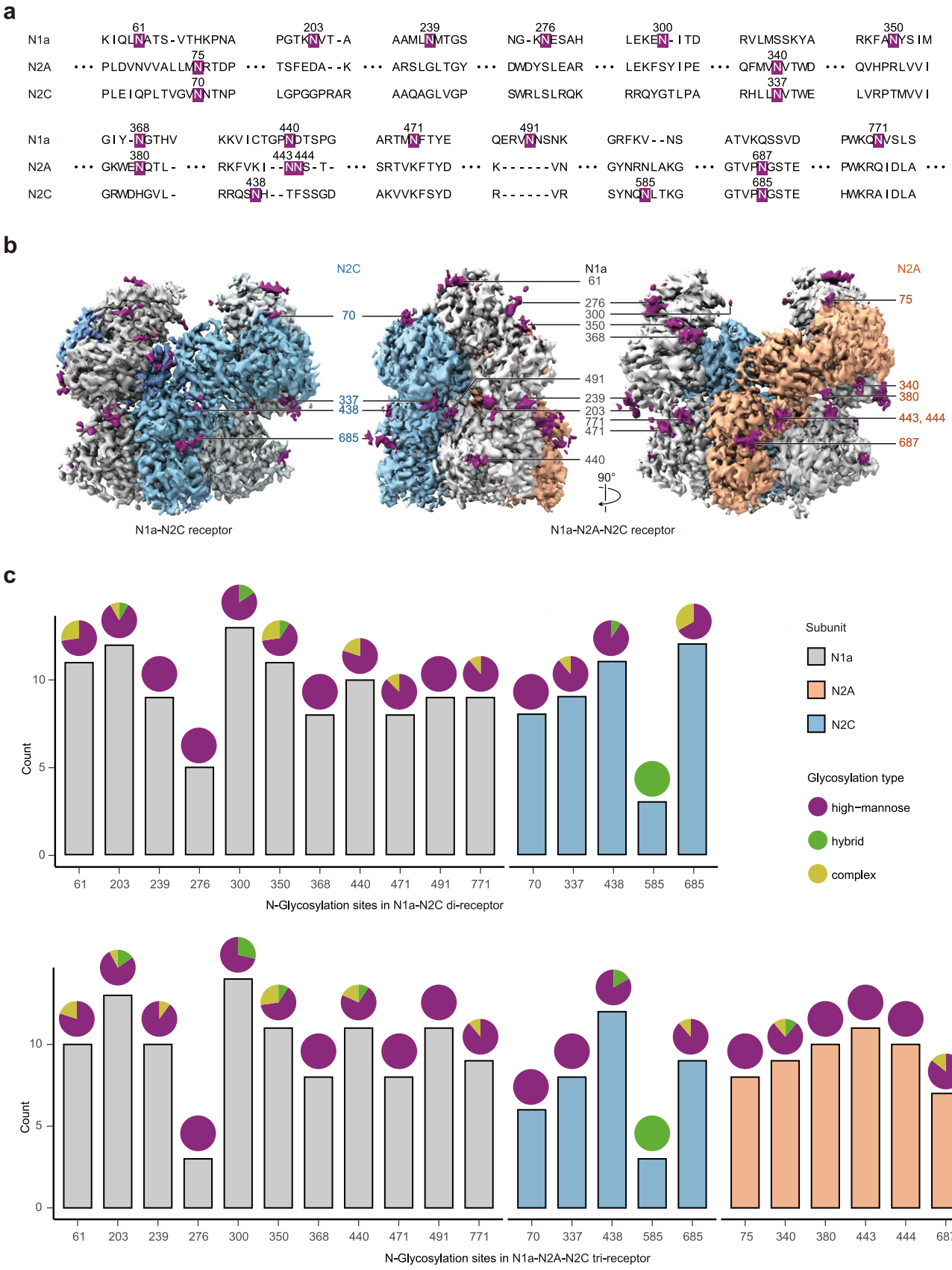

Extended Data Fig. 6 | N-linked glycosylation analysis by mass spectrometry. **a**, Sequence alignment of the *Rat norvegicus* N1a, N2A and N2C subunits, highlighted the sites (in purple) detected with N-glycosylation modifications by mass spectrometry. **b**, Glycans signal (in purple) on EM density maps of N1-N2C (major class) and N1-N2A-N2C receptors are marked. Residue N2C^{N585} located on the intracellular loop between TM1 and TM2 helices, was detected with N-glycosylation modifications, but not present on the map. **c**, Statistical chart of site-specified N-glycosylation in N1-N2C di-receptors and N1-N2A-N2C tri-receptors by mass spectrometry. The bar plot summarizes the total count of the different N-glycan compositions, and the pie charts summarize the count distribution of different N-glycosylation types for each N-glycosylated site.

https://doi.org/10.1038/s41594-023-00959-z

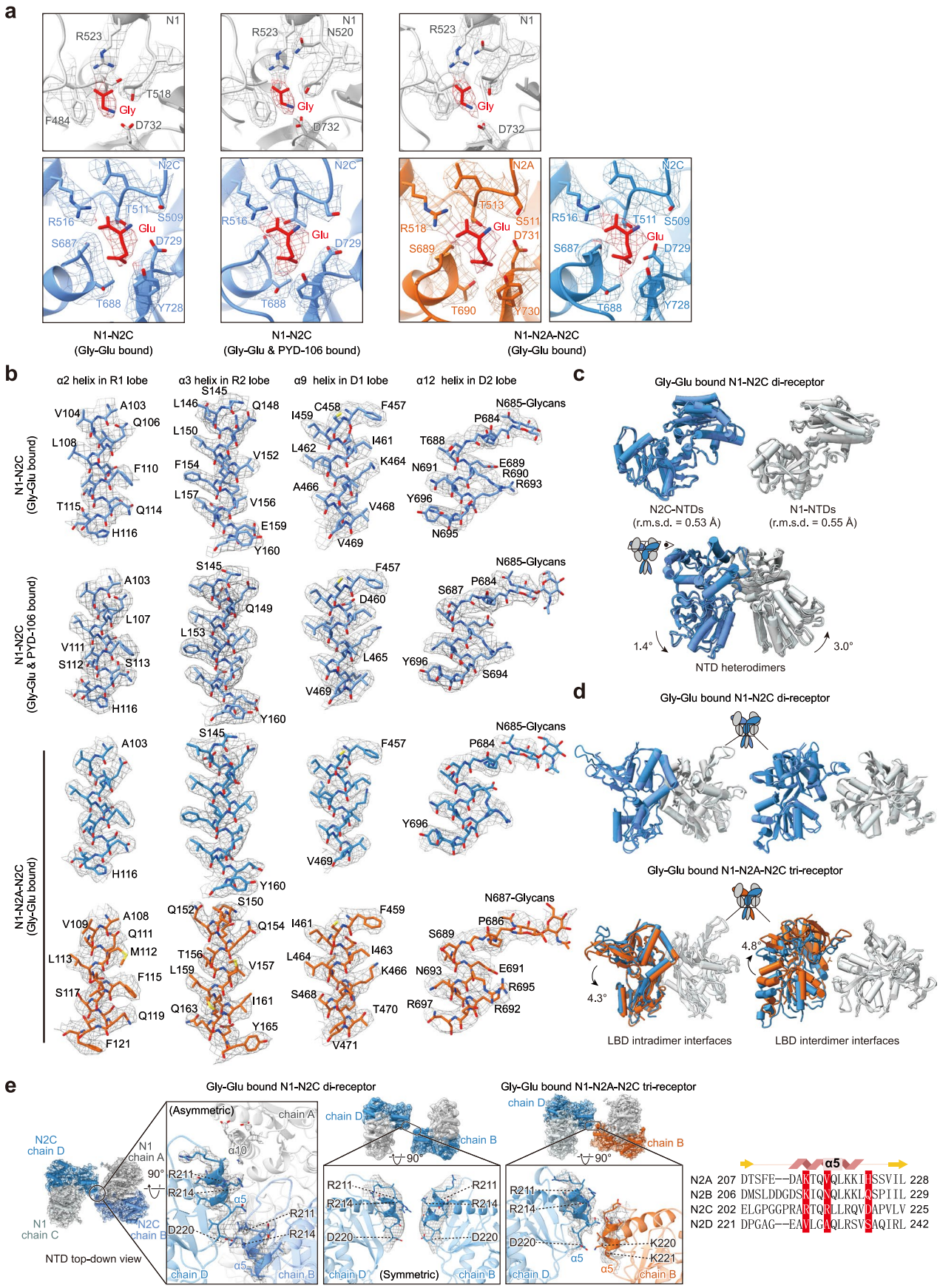

Extended Data Fig. 7 | See next page for caption.

https://doi.org/10.1038/s41594-023-00959-z

Extended Data Fig. 7 | Cryo-EM density maps and structural comparisons of N1-N2C and N1-N2A-N2C receptors. a, **b**, Electron density of ligands at the LBD clamshells are shown in red mesh (**a**). Representative local densities of N2 subunits in Gly-Glu bound (major class) or PYD-106 bound N1-N2C di-receptors, and N1-N2A-N2C tri-receptor structures (**b**). The models are shown as cartoons and residues are shown as sticks, with N1 coloured in grey, N2A in orange, N2C (chain B) in grey blue and N2C (chain D) in light blue. Agonists Gly and Glu are shown in red sticks. **c**, Structural comparisons of NTDs and NTD heterodimers within the major class of Gly-Glu bound N1-N2C di-receptor. The r.m.s.d for NTD alignment of N2C (chain B *vs* chain D) and N1 (chain A *vs* chain C) are indicated. NTD heterodimers were superimposed using the R1 lobes of N1 with the rotation angles of R2 lobes indicated. **d**, Structural comparisons of LBD intra-dimer and inter-dimer with the N1-LBDs aligned within the N1-N2C di- (major class, top panel) or N1-N2A-N2C tri-receptors (bottom panel). Rotation angles of N2-LBDs (from N2C to N2A) in the tri-receptor are indicated. Overall, LBDs exhibit pseudo-symmetry in N1-N2C di-receptor and asymmetry in N1-N2A-N2C tri-receptors. **e**, Arrangement of the NTD tetrameric interface in the asymmetric or symmetric class of N1-N2C di- and N1-N2A-N2C tri-receptors. Three N2C-specific residues (R211, R214 and D220) located at α-helix 5 mediating ionic bond interaction are shaded in red in the sequence alignment of *Rat norvegicus* N2 subunits at right panel.

https://doi.org/10.1038/s41594-023-00959-z

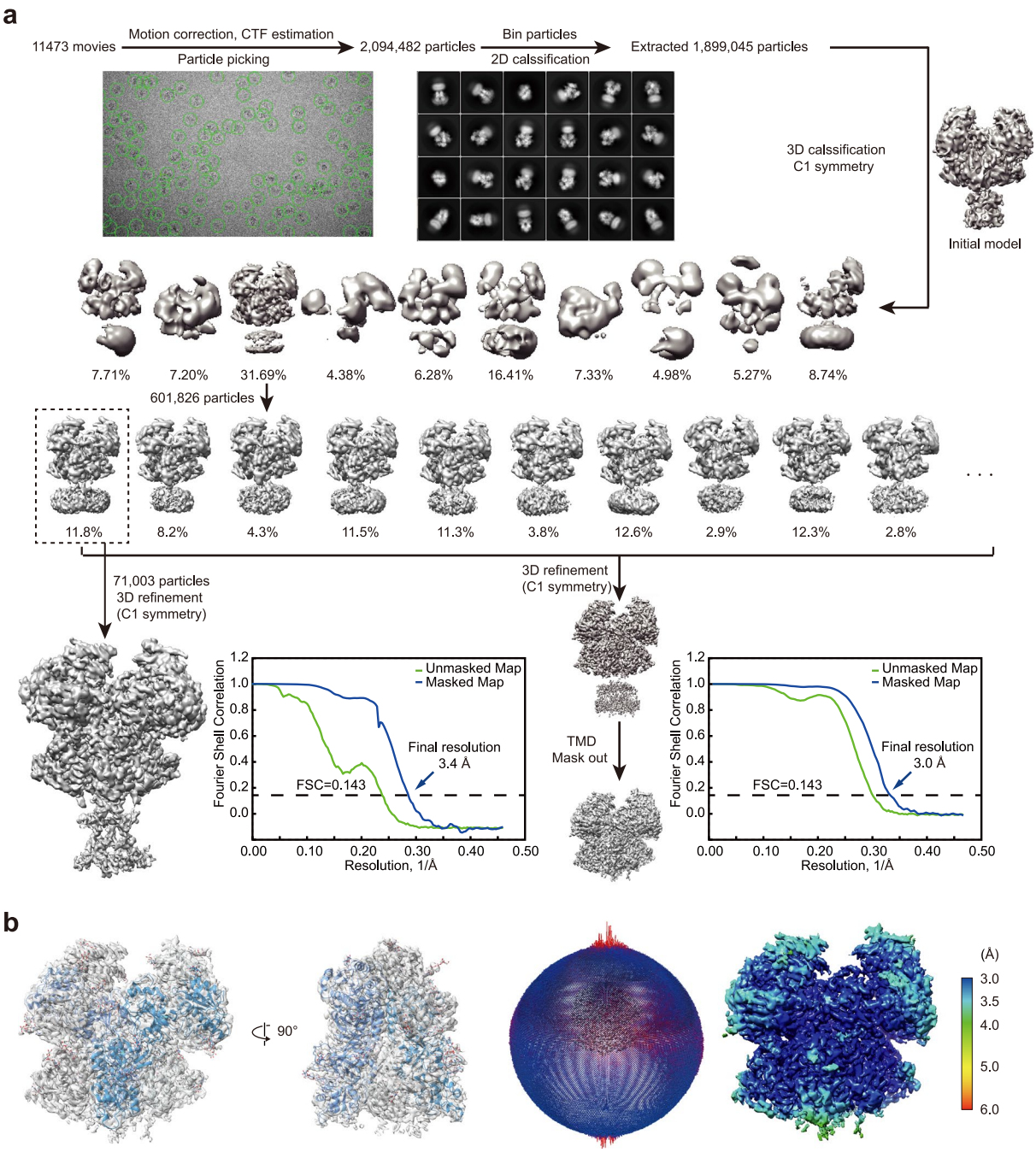

Extended Data Fig. 8 | Cryo-EM data processing of N1-N2C di-receptors in PYD-106 bound state. a, Cryo-EM data-processing flowchart of N1-N2C receptors in complex with Gly-Glu & PYD-106. Representative micrographs, 2D class average images and 3D classification maps are shown. To push the resolution of ECD, focused refinement was conducted on the PYD-106 bound N1-N2C receptor, with TMD masked out. For the same purpose, one class of best TMD signal was also processed individually to get a map displaying certain signal of TMD. Masked (blue) and unmasked (green) FSCs of corresponding maps are both shown, with gold standard FSC of 0.143 criteria indicated. **b**, Representation of model fit to map, the angular distribution of particles used in the final reconstruction are shown.

https://doi.org/10.1038/s41594-023-00959-z

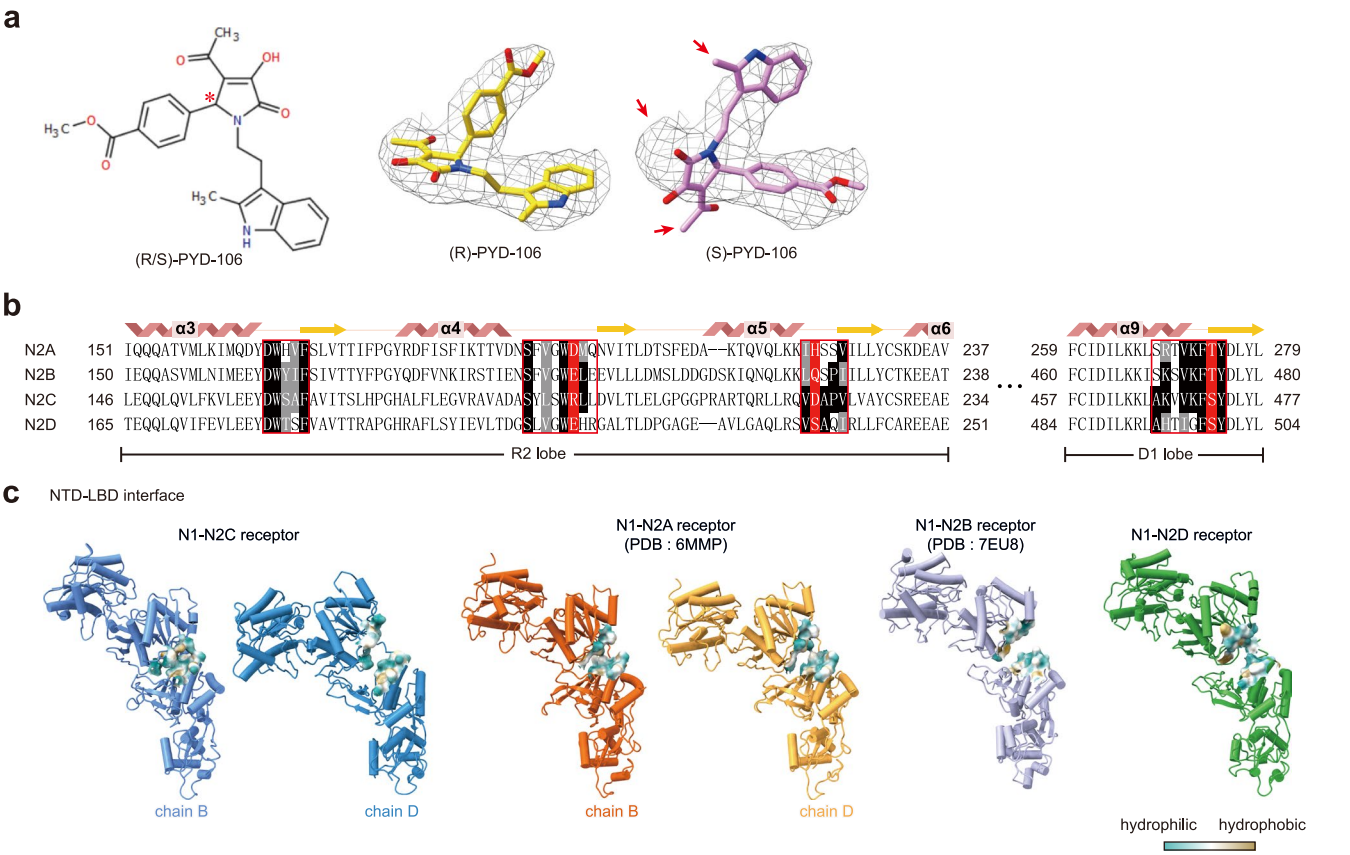

Extended Data Fig. 9 | Molecular mechanism of PYD-106 selectivity on N1-N2C di-receptors. a, Structural formula of PYD-106 with the only chiral carbon atom in the molecule marked with a red asterisk and the fits of (*R*)- and (*S*)-PYD-106 into the EM map which is shown in mesh. Red arrows indicate the unfavorable fitting for (*S*)-PYD-106. **b**, Sequence alignment of *Rat norvegicus* N2A, N2B, N2C and N2D subunits. Red boxes indicate the homologous residues at the bottom of the R2 lobe and the top of the D1 lobe, which directly interact with PYD-106 in Ligplot^{+} in N2C (chain B). Three key residues that form hydrogen bonds with PYD-106 in N2C (R194, D220 and S472) and their homologous residues are highlighted in red. **c**, Comparison of the NTD-LBD interfaces of N2 subunits in N1-N2C, N1-N2A (PDB:6MMP, ref. [22]), N1-N2B (PDB:7EU8, ref. [26]) and N1-N2D di-receptors. The hydrophobicity feature of NTD-LBD interface is highlighted with residues at R2 and D1 lobes.

https://doi.org/10.1038/s41594-023-00959-z

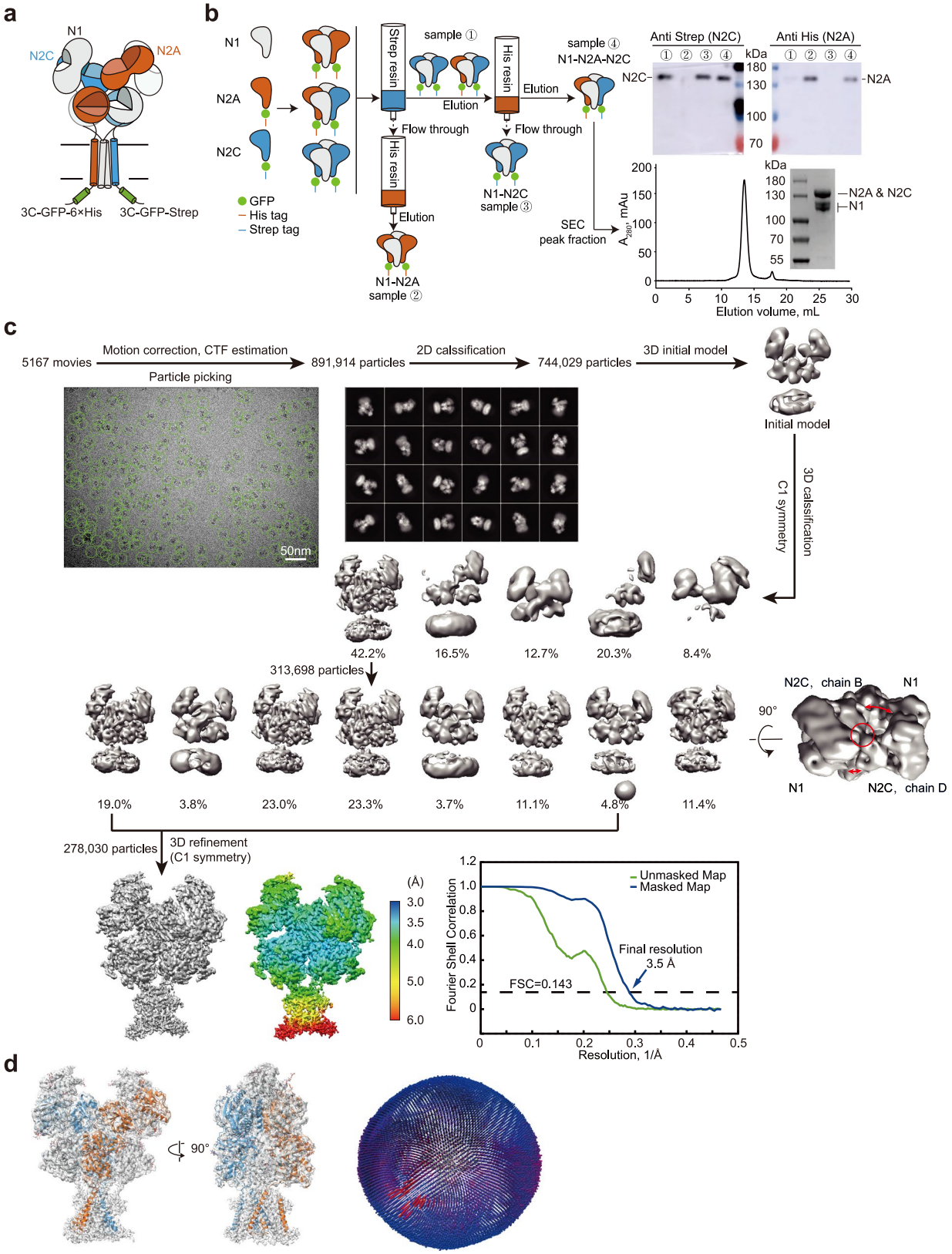

Extended Data Fig. 10 | See next page for caption.

https://doi.org/10.1038/s41594-023-00959-z

Extended Data Fig. 10 | Purification, biochemical and cryo-EM analysis of the N1-N2A-N2C tri-receptor. a, Cartoon representation of N1-N2A-N2C tri-receptor, with GFP-6×His tag and GFP-Strep Tag placed at the C terminus of N2A and N2C constructs, respectively. **b**, Pipeline of two-step affinity chromatography shows that elution of Strep resin was further purified by His resin. Schematic indicates the putative receptor types existed during purification process. Subunit composition at each step was verified by western blotting analysis and the presence of both N2A and N2C subunits was confirmed in the sample after Strep and His affinity purification successively. FSEC profile and Coomassie blue gel staining for the purified tri-receptor protein are shown. Gel and FSEC analysis were repeated three times. **c**, Flowchart of cryo-EM data-processing for Gly-Glu bound N1-N2A-N2C tri-receptor. The initial model was generated *de novo* from the selected 2D particles in Relion 3.1.1[50]. One distinctive 3D class (occupied 11.4% particles) showed N1-N2C di-receptor (major class) liked asymmetric features, which was not considered for final 3D refinement. Masked (blue) and unmasked (green) FSCs of corresponding maps are both shown, with gold standard FSC of 0.143 criteria indicated. **d**, Representation of model fit to map and the angular distribution of particles used in the final reconstruction were shown.

nature portfolio

Corresponding author(s): Shujia Zhu

Last updated by author(s): Feb 12, 2023

Reporting Summary

Nature Portfolio wishes to improve the reproducibility of the work that we publish. This form provides structure for consistency and transparency in reporting. For further information on Nature Portfolio policies, see our Editorial Policies and the Editorial Policy Checklist.

Statistics

For all statistical analyses, confirm that the following items are present in the figure legend, table legend, main text, or Methods section.

n/a	Confirmed
☐	☒ The exact sample size (*n*) for each experimental group/condition, given as a discrete number and unit of measurement
☐	☒ A statement on whether measurements were taken from distinct samples or whether the same sample was measured repeatedly
☐	☒ The statistical test(s) used AND whether they are one- or two-sided *Only common tests should be described solely by name; describe more complex techniques in the Methods section.*
☒	☐ A description of all covariates tested
☐	☒ A description of any assumptions or corrections, such as tests of normality and adjustment for multiple comparisons
☐	☒ A full description of the statistical parameters including central tendency (e.g. means) or other basic estimates (e.g. regression coefficient) AND variation (e.g. standard deviation) or associated estimates of uncertainty (e.g. confidence intervals)
☐	☒ For null hypothesis testing, the test statistic (e.g. *F*, *t*, *r*) with confidence intervals, effect sizes, degrees of freedom and *P* value noted *Give P values as exact values whenever suitable.*
☒	☐ For Bayesian analysis, information on the choice of priors and Markov chain Monte Carlo settings
☒	☐ For hierarchical and complex designs, identification of the appropriate level for tests and full reporting of outcomes
☒	☐ Estimates of effect sizes (e.g. Cohen's *d*, Pearson's *r*), indicating how they were calculated

Our web collection on statistics for biologists contains articles on many of the points above.

Software and code

Policy information about availability of computer code

Data collection	Clampex 10.6 Patchmaster v2x90.3 was used for electrophysiological data collection. Serial EM 3.7.11 were used for Cryo-EM image collection.
Data analysis	Clampfit 10.7 and GraphPad Prism 8.0 were used for electrophysiological recordings and data analysis. Relion 3.1.1, CryoSPARC 3.0, MotionCor2 1.4.0, Gctf_v1.06 and ResMap-1.1.4 were used for Cryo-EM image analysis. Phenix 1.20.1, Coot 0.9.6.1, ChimeraX 1.14 and Pymol 2.5.2 were used for model determination, refinement and analysis of structures. Maestro, CHARMM-GUI and GROMACS26 version 2021.3 program package were used for structure refinement, simulation system construction and molecular dynamics (MD) simulation. The results of MD simulation were analyzed by Gromacs tools and VMD 1.9.4. Program gmmpbsa v1.6 was used for per-residue decomposition energy calculation. Mass spectrometry data were processed by pGlyco 3.0.

For manuscripts utilizing custom algorithms or software that are central to the research but not yet described in published literature, software must be made available to editors and reviewers. We strongly encourage code deposition in a community repository (e.g. GitHub). See the Nature Portfolio guidelines for submitting code & software for further information.

Data

Policy information about availability of data

All manuscripts must include a data availability statement. This statement should provide the following information, where applicable:

- Accession codes, unique identifiers, or web links for publicly available datasets
- A description of any restrictions on data availability
- For clinical datasets or third party data, please ensure that the statement adheres to our policy

Data availability
Cryo-EM density maps and structural coordinates have been deposited in the Electron Microscopy Database and Protein Data Bank under accession codes of EMD-33792 and 7YFL for Gly-Glu bound N1a-N2D, EMD-33788 and 7YFF for Gly-CPP bound N1a-N2D, EMD-33795 and 7YFO for crosslinked N1aE698C-N2D, EMD-33798 and 7YFR for non-crosslinked N1aE698C-N2D, EMD-33793 and 7YFM for Gly-Glu bound N1b-N2D, EMD-33789 and 7YFG for Gly-Glu bound N1a-N2C in asymmetric conformation, EMD-34674 and 8HDK for Gly-Glu bound N1a-N2C in symmetric conformation, EMD-33790 and 7YFH for PYD-106 bound N1a-GluN2C, EMD-33791 and 7YFI for Gly-Glu bound N1a-N2A-N2C receptors, respectively. Additional data that support the findings of this study are available from the corresponding author upon request. Source data are provided with this paper.

Human research participants

Policy information about studies involving human research participants and Sex and Gender in Research.

Reporting on sex and gender	n/a
Population characteristics	n/a
Recruitment	n/a
Ethics oversight	n/a

Note that full information on the approval of the study protocol must also be provided in the manuscript.

Field-specific reporting

Please select the one below that is the best fit for your research. If you are not sure, read the appropriate sections before making your selection.

☒ Life sciences ☐ Behavioural & social sciences ☐ Ecological, evolutionary & environmental sciences

For a reference copy of the document with all sections, see nature.com/documents/nr-reporting-summary-flat.pdf

Life sciences study design

All studies must disclose on these points even when the disclosure is negative.

Sample size	The number of micrographs collected and particles included in final cryo-EM structures are mentioned in the legend of Extended Data Fig.1, 2, 4, 5, 8, 10. And the number are commonly sufficient in the field of cryo-EM. The number of oocytes or proteoliposomes were mentioned in the legends of Figure 2 and Extended Data Fig.3. TEVC recordings were repeated at least three times on independent oocytes and single-channel recordings were repeated six times on independent proteoliposomes. These numbers are commonly sufficient in the field of electrophysiology.
Data exclusions	Micrographs and particles that did not contribute to high resolution structure determination were excluded during data processing, which is a standard procedure during the cryo-EM structural determination. No data was excluded in electrophysiology analysis.
Replication	Protein expression, purification, and cryo-EM sample preparation were reproduced at least three times independently. For gel electrophoresis analysis and western blot, multiple batches (at least three times repeated) of experiments were performed to ensure the reproducibility. TEVC recordings were repeated at least on three independent xenopus oocytes and single-channel recordings were repeated six times on different proteoliposomes incorporated with NMDA receptors. All electrophysiological experiments showed consistent results.
Randomization	Particles/images were randomly partitioned for resolution and quality assessment. Randomization serves no purpose in elecrophysiological experiments because the experimental conditions are systematic. Oocytes and proteoliposomes for electrophysiological recordings were chosen randomly.
Blinding	Blinding served no purpose for cryo-EM analysis, MD simulation and electrophysiological experiments since the analyses in all experiments are systematic and do not requires subjective assessment of the data.

Behavioural & social sciences study design

All studies must disclose on these points even when the disclosure is negative.

Study description	*Briefly describe the study type including whether data are quantitative, qualitative, or mixed-methods (e.g. qualitative cross-sectional, quantitative experimental, mixed-methods case study).*
Research sample	*State the research sample (e.g. Harvard university undergraduates, villagers in rural India) and provide relevant demographic information (e.g. age, sex) and indicate whether the sample is representative. Provide a rationale for the study sample chosen. For studies involving existing datasets, please describe the dataset and source.*
Sampling strategy	*Describe the sampling procedure (e.g. random, snowball, stratified, convenience). Describe the statistical methods that were used to predetermine sample size OR if no sample-size calculation was performed, describe how sample sizes were chosen and provide a rationale for why these sample sizes are sufficient. For qualitative data, please indicate whether data saturation was considered, and what criteria were used to decide that no further sampling was needed.*
Data collection	*Provide details about the data collection procedure, including the instruments or devices used to record the data (e.g. pen and paper, computer, eye tracker, video or audio equipment) whether anyone was present besides the participant(s) and the researcher, and whether the researcher was blind to experimental condition and/or the study hypothesis during data collection.*
Timing	*Indicate the start and stop dates of data collection. If there is a gap between collection periods, state the dates for each sample cohort.*
Data exclusions	*If no data were excluded from the analyses, state so OR if data were excluded, provide the exact number of exclusions and the rationale behind them, indicating whether exclusion criteria were pre-established.*
Non-participation	*State how many participants dropped out/declined participation and the reason(s) given OR provide response rate OR state that no participants dropped out/declined participation.*
Randomization	*If participants were not allocated into experimental groups, state so OR describe how participants were allocated to groups, and if allocation was not random, describe how covariates were controlled.*

Ecological, evolutionary & environmental sciences study design

All studies must disclose on these points even when the disclosure is negative.

Study description	*Briefly describe the study. For quantitative data include treatment factors and interactions, design structure (e.g. factorial, nested, hierarchical), nature and number of experimental units and replicates.*
Research sample	*Describe the research sample (e.g. a group of tagged Passer domesticus, all Stenocereus thurberi within Organ Pipe Cactus National Monument), and provide a rationale for the sample choice. When relevant, describe the organism taxa, source, sex, age range and any manipulations. State what population the sample is meant to represent when applicable. For studies involving existing datasets, describe the data and its source.*
Sampling strategy	*Note the sampling procedure. Describe the statistical methods that were used to predetermine sample size OR if no sample-size calculation was performed, describe how sample sizes were chosen and provide a rationale for why these sample sizes are sufficient.*
Data collection	*Describe the data collection procedure, including who recorded the data and how.*
Timing and spatial scale	*Indicate the start and stop dates of data collection, noting the frequency and periodicity of sampling and providing a rationale for these choices. If there is a gap between collection periods, state the dates for each sample cohort. Specify the spatial scale from which the data are taken*
Data exclusions	*If no data were excluded from the analyses, state so OR if data were excluded, describe the exclusions and the rationale behind them, indicating whether exclusion criteria were pre-established.*
Reproducibility	*Describe the measures taken to verify the reproducibility of experimental findings. For each experiment, note whether any attempts to repeat the experiment failed OR state that all attempts to repeat the experiment were successful.*
Randomization	*Describe how samples/organisms/participants were allocated into groups. If allocation was not random, describe how covariates were controlled. If this is not relevant to your study, explain why.*
Blinding	*Describe the extent of blinding used during data acquisition and analysis. If blinding was not possible, describe why OR explain why blinding was not relevant to your study.*

Did the study involve field work? ☐ Yes ☐ No

Field work, collection and transport

Field conditions	*Describe the study conditions for field work, providing relevant parameters (e.g. temperature, rainfall).*
Location	*State the location of the sampling or experiment, providing relevant parameters (e.g. latitude and longitude, elevation, water depth).*
Access & import/export	*Describe the efforts you have made to access habitats and to collect and import/export your samples in a responsible manner and in compliance with local, national and international laws, noting any permits that were obtained (give the name of the issuing authority, the date of issue, and any identifying information).*
Disturbance	*Describe any disturbance caused by the study and how it was minimized.*

Reporting for specific materials, systems and methods

We require information from authors about some types of materials, experimental systems and methods used in many studies. Here, indicate whether each material, system or method listed is relevant to your study. If you are not sure if a list item applies to your research, read the appropriate section before selecting a response.

Materials & experimental systems

n/a	Involved in the study
☐	☒ Antibodies
☐	☒ Eukaryotic cell lines
☒	☐ Palaeontology and archaeology
☒	☐ Animals and other organisms
☒	☐ Clinical data
☒	☐ Dual use research of concern

Methods

n/a	Involved in the study
☒	☐ ChIP-seq
☒	☐ Flow cytometry
☒	☐ MRI-based neuroimaging

Antibodies

Antibodies used	anti-GluN1 antibody: MAB1586, Millipore, Clone R1JHL, 1:1000 dilution; anti-GluN2D antibody: MAB5578, Millipore,Clone 1G9.39A5, 1:500 dilution; anti-Strep antibody: ab252885, Abcam, Clone 11A7, 1:1000 dilution; anti-His antibody: ab15149, Abcam, Clone AD1.1.10, 1:1000 dilution; HRP-conjugated anti mouse IgG antibody: Cell Signaling Technology, 7076s, 1:4000 dilution; HRP-conjugated anti rabbit IgG antibody: Cell Signaling Technology, 7074P2, 1:4000 dilution. All antibodies used were diluted in 5% defatted milk powder TBST buffer.
Validation	All antibodies were commercially obtained and validation reports are available on the supplier website. For details: Anti-GluN1 antibody (MAB1586, Millipore) was validated for using in western blot to detect GluN1 (reactive with all splicing variants of Human, Mouse and Rat species). No cross-reactivity observed with other NMDA receptor subunits. Recognizes a ~120 kDa protein in rat brain hippocampal homogenate by immunoblot. Anti-GluN2D antibody (MAB5578, Millipore) was validated for using in western blot to detect the C-terminal of GluN2D subunit, (reactive with Human, Mouse, Rat and Rabbit species). The antibody reacts with the protein showing a weak band at ~145 kDa. A non-specific band at ~75 kDa may be seen depending on sample and antibody concentration used. Anti-Strep-tag II antibody (ab252885) was validated by western blot using strep-tagged standard marker. Anti-His-tag antibody (ab15149) was validated by western blot using His-tagged protein.

Eukaryotic cell lines

Policy information about cell lines and Sex and Gender in Research

Cell line source(s)	The sf9 insect cells (CRL-1711, ATCC) and HEK293S GnTI- cells (CRL-3022, ATCC) were general gifts from the laboratory of Prof. Eric Gouaux (Vollum Institute, Portland, USA).
Authentication	The cells were routinely maintained in our laboratory. They were not authenticated for these studies.
Mycoplasma contamination	The cell lines were tested negative for mycoplasma contamination.
Commonly misidentified lines (See ICLAC register)	No commonly misidentified cell lines were used.

Palaeontology and Archaeology

Specimen provenance	*Provide provenance information for specimens and describe permits that were obtained for the work (including the name of the issuing authority, the date of issue, and any identifying information). Permits should encompass collection and, where applicable, export.*
Specimen deposition	*Indicate where the specimens have been deposited to permit free access by other researchers.*
Dating methods	*If new dates are provided, describe how they were obtained (e.g. collection, storage, sample pretreatment and measurement), where they were obtained (i.e. lab name), the calibration program and the protocol for quality assurance OR state that no new dates are provided.*

☐ Tick this box to confirm that the raw and calibrated dates are available in the paper or in Supplementary Information.

Ethics oversight	*Identify the organization(s) that approved or provided guidance on the study protocol, OR state that no ethical approval or guidance was required and explain why not.*

Note that full information on the approval of the study protocol must also be provided in the manuscript.

Animals and other research organisms

Policy information about studies involving animals; ARRIVE guidelines recommended for reporting animal research, and Sex and Gender in Research

Laboratory animals	*For laboratory animals, report species, strain and age OR state that the study did not involve laboratory animals.*
Wild animals	*Provide details on animals observed in or captured in the field; report species and age where possible. Describe how animals were caught and transported and what happened to captive animals after the study (if killed, explain why and describe method; if released, say where and when) OR state that the study did not involve wild animals.*
Reporting on sex	*Indicate if findings apply to only one sex; describe whether sex was considered in study design, methods used for assigning sex. Provide data disaggregated for sex where this information has been collected in the source data as appropriate; provide overall numbers in this Reporting Summary. Please state if this information has not been collected. Report sex-based analyses where performed, justify reasons for lack of sex-based analysis.*
Field-collected samples	*For laboratory work with field-collected samples, describe all relevant parameters such as housing, maintenance, temperature, photoperiod and end-of-experiment protocol OR state that the study did not involve samples collected from the field.*
Ethics oversight	*Identify the organization(s) that approved or provided guidance on the study protocol, OR state that no ethical approval or guidance was required and explain why not.*

Note that full information on the approval of the study protocol must also be provided in the manuscript.

Clinical data

Policy information about clinical studies

All manuscripts should comply with the ICMJE guidelines for publication of clinical research and a completed CONSORT checklist must be included with all submissions.

Clinical trial registration	*Provide the trial registration number from ClinicalTrials.gov or an equivalent agency.*
Study protocol	*Note where the full trial protocol can be accessed OR if not available, explain why.*
Data collection	*Describe the settings and locales of data collection, noting the time periods of recruitment and data collection.*
Outcomes	*Describe how you pre-defined primary and secondary outcome measures and how you assessed these measures.*

Dual use research of concern

Policy information about dual use research of concern

Hazards

Could the accidental, deliberate or reckless misuse of agents or technologies generated in the work, or the application of information presented in the manuscript, pose a threat to:

No	Yes	
☐	☐	Public health
☐	☐	National security
☐	☐	Crops and/or livestock
☐	☐	Ecosystems
☐	☐	Any other significant area

Experiments of concern

Does the work involve any of these experiments of concern:

No	Yes	
☐	☐	Demonstrate how to render a vaccine ineffective
☐	☐	Confer resistance to therapeutically useful antibiotics or antiviral agents
☐	☐	Enhance the virulence of a pathogen or render a nonpathogen virulent
☐	☐	Increase transmissibility of a pathogen
☐	☐	Alter the host range of a pathogen
☐	☐	Enable evasion of diagnostic/detection modalities
☐	☐	Enable the weaponization of a biological agent or toxin
☐	☐	Any other potentially harmful combination of experiments and agents

ChIP-seq

Data deposition

☐ Confirm that both raw and final processed data have been deposited in a public database such as GEO.

☐ Confirm that you have deposited or provided access to graph files (e.g. BED files) for the called peaks.

Data access links *May remain private before publication.*	*For "Initial submission" or "Revised version" documents, provide reviewer access links. For your "Final submission" document, provide a link to the deposited data.*
Files in database submission	*Provide a list of all files available in the database submission.*
Genome browser session (e.g. UCSC)	*Provide a link to an anonymized genome browser session for "Initial submission" and "Revised version" documents only, to enable peer review. Write "no longer applicable" for "Final submission" documents.*

Methodology

Replicates	*Describe the experimental replicates, specifying number, type and replicate agreement.*
Sequencing depth	*Describe the sequencing depth for each experiment, providing the total number of reads, uniquely mapped reads, length of reads and whether they were paired- or single-end.*
Antibodies	*Describe the antibodies used for the ChIP-seq experiments; as applicable, provide supplier name, catalog number, clone name, and lot number.*
Peak calling parameters	*Specify the command line program and parameters used for read mapping and peak calling, including the ChIP, control and index files used.*
Data quality	*Describe the methods used to ensure data quality in full detail, including how many peaks are at FDR 5% and above 5-fold enrichment.*
Software	*Describe the software used to collect and analyze the ChIP-seq data. For custom code that has been deposited into a community repository, provide accession details.*

Flow Cytometry

Plots

Confirm that:

☐ The axis labels state the marker and fluorochrome used (e.g. CD4-FITC).

☐ The axis scales are clearly visible. Include numbers along axes only for bottom left plot of group (a 'group' is an analysis of identical markers).

☐ All plots are contour plots with outliers or pseudocolor plots.

☐ A numerical value for number of cells or percentage (with statistics) is provided.

Methodology

Sample preparation	*Describe the sample preparation, detailing the biological source of the cells and any tissue processing steps used.*
Instrument	*Identify the instrument used for data collection, specifying make and model number.*
Software	*Describe the software used to collect and analyze the flow cytometry data. For custom code that has been deposited into a community repository, provide accession details.*
Cell population abundance	*Describe the abundance of the relevant cell populations within post-sort fractions, providing details on the purity of the samples and how it was determined.*
Gating strategy	*Describe the gating strategy used for all relevant experiments, specifying the preliminary FSC/SSC gates of the starting cell population, indicating where boundaries between "positive" and "negative" staining cell populations are defined.*

☐ Tick this box to confirm that a figure exemplifying the gating strategy is provided in the Supplementary Information.

Magnetic resonance imaging

Experimental design

Design type	*Indicate task or resting state; event-related or block design.*
Design specifications	*Specify the number of blocks, trials or experimental units per session and/or subject, and specify the length of each trial or block (if trials are blocked) and interval between trials.*
Behavioral performance measures	*State number and/or type of variables recorded (e.g. correct button press, response time) and what statistics were used to establish that the subjects were performing the task as expected (e.g. mean, range, and/or standard deviation across subjects).*

Acquisition

Imaging type(s)	*Specify: functional, structural, diffusion, perfusion.*
Field strength	*Specify in Tesla*
Sequence & imaging parameters	*Specify the pulse sequence type (gradient echo, spin echo, etc.), imaging type (EPI, spiral, etc.), field of view, matrix size, slice thickness, orientation and TE/TR/flip angle.*
Area of acquisition	*State whether a whole brain scan was used OR define the area of acquisition, describing how the region was determined.*

Diffusion MRI ☐ Used ☐ Not used

Preprocessing

Preprocessing software	*Provide detail on software version and revision number and on specific parameters (model/functions, brain extraction, segmentation, smoothing kernel size, etc.).*
Normalization	*If data were normalized/standardized, describe the approach(es): specify linear or non-linear and define image types used for transformation OR indicate that data were not normalized and explain rationale for lack of normalization.*
Normalization template	*Describe the template used for normalization/transformation, specifying subject space or group standardized space (e.g. original Talairach, MNI305, ICBM152) OR indicate that the data were not normalized.*
Noise and artifact removal	*Describe your procedure(s) for artifact and structured noise removal, specifying motion parameters, tissue signals and physiological signals (heart rate, respiration).*

Volume censoring

Define your software and/or method and criteria for volume censoring, and state the extent of such censoring.

Statistical modeling & inference

Model type and settings

Specify type (mass univariate, multivariate, RSA, predictive, etc.) and describe essential details of the model at the first and second levels (e.g. fixed, random or mixed effects; drift or auto-correlation).

Effect(s) tested

Define precise effect in terms of the task or stimulus conditions instead of psychological concepts and indicate whether ANOVA or factorial designs were used.

Specify type of analysis: ☐ Whole brain ☐ ROI-based ☐ Both

Statistic type for inference
(See Eklund et al. 2016)

Specify voxel-wise or cluster-wise and report all relevant parameters for cluster-wise methods.

Correction

Describe the type of correction and how it is obtained for multiple comparisons (e.g. FWE, FDR, permutation or Monte Carlo).

Models & analysis

n/a	Involved in the study
☐	☐ Functional and/or effective connectivity
☐	☐ Graph analysis
☐	☐ Multivariate modeling or predictive analysis

Functional and/or effective connectivity

Report the measures of dependence used and the model details (e.g. Pearson correlation, partial correlation, mutual information).

Graph analysis

Report the dependent variable and connectivity measure, specifying weighted graph or binarized graph, subject- or group-level, and the global and/or node summaries used (e.g. clustering coefficient, efficiency, etc.).

Multivariate modeling and predictive analysis

Specify independent variables, features extraction and dimension reduction, model, training and evaluation metrics.